Simulation of Adaptive Antenna Array Implementation for Low Earth Orbit Constellation Tracking

SIMULATION OF ADAPTIVE ANTENNA ARRAY IMPLEMENTATION FOR LOW EARTH ORBIT CONSTELLATION TRACKING

by

SYAZANA BASYIRAH BINTI MOHAMMAD ZAKI

16595907

Applied Science for Integrated Systems Engineering

in Department of Engineering

Graduate School of Engineering

Kyushu Institute of Technology

Thesis submitted in fulfillment of the requirements

for the degree of

Doctor of Philosophy in Engineering

August, 2020

ABSTRACT

Since Low Earth Orbit has become an in orbit to place satellites, CubeSat constellation tracking is challenging. Higher capacity and capability of a new Ground Station tracking system are in demand and this, motivates researchers to come out with a solution to mitigate the traditional Ground Station degradation performance. This paper discusses the Least Mean Square algorithm's implementation in Adaptive Array Antenna for the Ground Station tracking system application. The simulation results show the capability of the main beam pattern to perform instantaneous tracking and steering towards the targeted CubeSat while suppressing the side lobes towards the other interfering CubeSats when a massive CubeSats constellation take place. Planar and circular array antennas are analyzed by setting the optimum weighting factors to be adapted. Three scenarios of CubeSats constellations are simulated. The performance of the Adaptive Array Antenna for each scenario is analyzed based on the beam width characteristics and the Signal-to-Interference Ratio of the beam pattern. The number of CubeSats tracked by the Adaptive Array Antenna and the capability of the system to perform fast-tracking as the number of antenna array elements is increased also discussed in this paper. Finally, solutions to mitigate the limitation of the Least Mean Square algorithm to perform fast-tracking when massive interferer CubeSats are nearby are proposed.

ACKNOWLEDGMENT

It is with the deepest sense of gratitude to the Almighty ALLAH who gives me strength and ability that I have now finally completed my research. All good aspirations, devotions and hardwork are due to His blessings. First and foremost, I wish to express my sincere appreciation to my supportive and talented supervisor, Professor Dr. Mengu Cho who was instrumental in providing opportunity, guidance, and supervision throughout conducting this research. The completion of this dissertation would also not be possible without the help from my co-supervisor Professor Nobuyuki Kaya who has been willing to assist me in the comprehension and application of the adaptive array antenna concepts every single step of the way. Special thanks to the Ministry of Higher Education Malaysia and Universiti Teknologi MARA for giving me the opportunity to pursue my studies in Japan and be a part of the BIRDS-2 Project and consequently obtain my Doctoral degree. I am forever in debt to the Yang Berbahagia Profesor Emeritus Dato' Dr. Hassan bin Said (former UiTM Vice-Chancellor) and Associate Professor Dr. Huzaimy bin Jusoh for their brilliant ideas and continuous support in the challenging BIRDS-2 Project journey. UiTM was then able to launch the first Malaysia's nanosatellite and develop space program and human capacity in the university. Being part of the BIRDS-2 while simultaneously carrying out this research, I was able to broaden my knowledge related to systems engineering, project management, space environment and team coordination. My appreciation also goes to BIRDS-2 members, Dr. Hirokazu Masui and Dr. Sangkyun Kim for their continuous support in the BIRDS-2 Project. Their experiences and continuous guidance helped in shaping the BIRDS-2 Project to the level that we can be proud of. Special thanks to all members of the Laboratory of Space Environment Interaction Engineering (LaSEINE) for their recommendations to improve this research. Not forgetting, Mr. George Maeda and secretaries of LaSEINE, Mr. Seichi Kawano, Ms. Sayo Tsukinari, and Ms. Kumiko Shirakawa, for making life in the laboratory an exciting working place. Special thanks to BIRDS partners and the Centre for Satellite Communication, FKE UiTM for supporting this research. I am also indebted to my beloved parents, relatives and friends for their prayers, love and continued support during my PhD journey. Last but not least, I thank my dear husband, Akmal, for showing extraordinary patience and being with me through thick and thin to ensure my success. This dissertation is dedicated to my beloved daughter, Raeesa Medina who has been my source of inspiration. A part of this work was supported by "Coordination Funds for Promoting AeroSpace Utilization", the Ministry of Education, Culture, Sports, Science and Technology (MEXT), Japan.

TABLE OF CONTENTS

LIST OF FIGURES

LIST OF TABLES

LIST OF ABBREVIATIONS

A

AAA – Adaptive Antenna Array

A/D – Analog/Digital

AF – Array Factor

AGI – Analytical Graphics, Inc.

AER – Azimuth Elevation Range

AOS – Acquisition of Signal

B

BPSK – Binary Phase Shift Keying

C

CPU – Central Processing Unit

D

DOA – Direction of Arrival

G

GS – Ground Station

I

ID – Identification

K

Kyutech – Kyushu Institute of Technology

L

LaSEINE – Laboratory of Space Environment Interaction Engineering

LEO – Low Earth Orbit

LMS – Least Mean Square

LOS – Loss of Signal

M

MATLAB – Matrix Laboratory

MSE – Mean Square Error

MT – Mobile Terminals

MSS – Mobile Satellite Systems

MUSIC – Multiple Signal Classification

ESPRIT – Estimation of Signal Parameter via Rotational Invariance Techniques

MMICs – Microwave Monolithic Integrated Circuits

R

RF – Radio Frequency

RLS – Recursive-Least-Squares

S

SIR – Signal-to-Interference Ratio

SOI – Signal-of-Interest

SNOI – Signal-of-Not-Interest

SPAAs – Spherical Phased Array Antennas

STK – Systems Tool Kit

T

TLE – Two-Line Element

U

UiTM – Universiti Teknologi MARA

UTC – Universal Time Coordinated

CHAPTER 1

INTRODUCTION

1.1 Overview

Recently, deploying CubeSats' constellation in the Low Earth Orbit (LEO) has become a trend among CubeSats builders as the lean philosophy is adopted in design, build and launch CubeSats with less cost and fast delivery. Choosing LEO to deploy CubeSats constellations offer an advantage because the orbit is dramatically closer to Earth, which benefits smaller satellites (like CubeSats) as they require less power. However, newer LEO CubeSats, mostly flying in constellations with a large quantity, add significant complexity and challenges to the tracking and communicating effort.

1.2 Problem Statement

A fast-tracking GS system is essential to perform tracking and communication for a massive LEO CubeSats constellation. Each singular CubeSat only has a line of sight to a GS for a short period, normally around 20 to 30 minutes during each pass [1]. This is due to the coverage area provided by a single LEO CubeSat only covers a small area that moves as the CubeSat travels at the high angular velocity needed to maintain its orbit. This requires a reliable GS antenna that can acquire the signal, track the CubeSat’s path, and upload or download as much data as possible within a short period. In the case of many CubeSats flying within each constellation, a higher capability of GS antenna is needed to be able to communicate through handoffs from one CubeSat to the next, and the other following CubeSats.

Apart from expensive, a mechanical GS antenna usually has slow movement which requires tens of seconds to locate and track a follow-on LEO CubeSats due to its large size and mechanical complexity to steer back/forth [1]. This significant constraint leads to incapability to perform multi-target tracking for CubeSats constellations, hence undesirable for data communications. Furthermore, the high duty cycle (constant movement and continual use) requires GS antennas that are rugged and high performing. As CubeSats in LEO are in constant motion as they orbit Earth, the mechanical GS antenna experience excessive wear and tear that comes from continual movement while tracking CubeSats after one and another. This significant degradation happens

when LEO GS tracking antennas move rapidly – both when tracking a LEO CubeSat from the horizon and when returning (retracing) to a position to link to the next CubeSat as it rises. These continual and rapid motions/movements experienced by the mechanical GS antenna contributes to significant mechanical performance degradation. These issues with the mechanical steering give rise to the need for a search for an alternative. By considering a smaller and lightweight type of antenna for tracking LEO CubeSats with no or minimal moving parts and mechanical stress, the reliability of a GS antenna can be increased.

The traditional GS tracking system faces significant performance degradation while tracking and performing communication with a targeted CubeSat when a massive LEO CubeSats constellation is within the same GS field of view. Once a CubeSat moves beyond the field of view, the GS antenna must seek a link to a different CubeSat that has come into the field of view and thus creates the inter-CubeSats signal interference and signal interference from the nearby CubeSats. At the GS side, the common traditional GS system is incapable to isolate these signals source from complex environment interference (it could be the signal source from nearby/other CubeSats or other signal sources even from the ground). The complex environment interference that occurs from the ground may lead to the GS degradation performance too. It is because the Direction of Arrival (DOA) signals from the targeted CubeSat could be hard to detect as the GS receives the same amount of electromagnetic waves (interference signal/multipath fading signal) from various directions. Besides interference on the ground side, the lower LEO CubeSats constellations also bring a serious in-line interference problem to CubeSat constellations network in the higher LEO during tracking and communicating. Thus, the emerging technology of the GS array antenna system which has the capability to perform precise tracking, adjust the direction of the main beam signal, enhancing the desired signal (towards the targeted CubeSat) and nulling out the interference signal is proposed in this study.

Because of these problems, higher capacity and capability of the GS tracking system are in demand and researchers are motivated to come out with a solution to cater to degradation performance at the GS side.

1.3 Research Objectives

The main objectives of this research are stated as follows:

1. To develop an LMS algorithm in AAA for GS tracking control system application.

2. To demonstrate the capability of electronically self-steering beampattern towards the desired signal while suppressing the other interferer signals.
3. To determine the DOAs of incoming signals.
4. To verify the performance of the LMS algorithm by analyzing the beampattern behavior, considering the real scenario of a massive LEO CubeSats constellations.

1.4 Research Scope

Since AAA covers wide fields, the scope range will be narrowed and focused on a specific aim. The scope of this dissertation will cover all objectives, focusing on the demonstration of the electronically self-steering for AAA control system which capable of the main beampattern towards the desired signal while suppressing the other interferer signals.

The LMS algorithm was implemented in the system for determining the DOA of the incoming signal from the targeted CubeSat. The weighting factors such as the step-size, number of elements, amplitude, phase and beam steering angle of the incident wave signal of the array antenna elements were adjusted, optimally.

Finally, the performance of the LMS algorithm was verified by analyzing the main beampattern behavior (narrow beamwidth for precise targeting), estimated Signal-to-Interference Ratio (SIR) calculated value (distinction of the desired signal to interference signal) and showing the ability of the LMS algorithm to perform fast-tracking with the optimum beam pattern (time taken by the system to calculate the new beam pattern for the next CubeSat's position), considering the real scenario of massive LEO CubeSats constellations.

1.5 Dissertation Organization

This dissertation was organized into five main chapters. Chapter 1 began with a discussion on challenges and complexity faced by newer LEO CubeSats players (from a GS tracking point of view) since massive constellations are now becoming a trend. The capability of the AAA system to perform the LEO CubeSat tracking system and the disadvantages of the existing traditional system were highlighted. The importance of having a reliable and high capacity GS system was described. The AAA system for a GS tracking system was introduced as an alternative replacement for the traditional GS system. Research objectives, problem statement and research scope of this research were stated at the end of this chapter. The remainder of this dissertation was structured as

follows. The general concept of AAA, LMS beamforming architecture of AAA and weight calculation from Steepest Descent Method derivation equations were explained in Chapter 2. The details on array factor equations of planar and circular array geometry were included. Several relevant literature reviews proposed by other researchers on the implementation of the steepest descent algorithm, smart signal processing algorithm in adaptive array antenna and phased array antenna for on-board satellite applications were mentioned at the end of Chapter 2.

Orbital analysis for massive constellation simulated in Analytical Graphics, Inc.'s (AGI's) Systems Tool Kit (STK) software for three scenarios of the constellation was presented in Chapter 3.

The simulation of orbital model and LEO CubeSat constellation interference and analysis on different scenarios of LEO constellations were discussed in Chapter 4. Simulation results of LMS algorithm and the analysis of its performance was also discussed in this chapter.

Finally, the importance of this research was elaborated in the Conclusion part of Chapter 5. Suggestion on the potential applications, improvement and extension of the system was finally, concluded.

CHAPTER 2

THEORETICAL BACKGROUND AND LITERATURE REVIEW

2.1 Overview

This chapter evolves towards the overview of the research for the implementation of an adaptive antenna array for the ground station tracking system. Here, the theoretical background was divided into several sections which include topics and subtopics in detail. To achieve the objectives of this research, the theoretical background part is focused mainly on the principle operation of an adaptive array antenna, beamforming architecture and detail weight calculation from the steepest descent method. Furthermore, the response of an array factor for two types of array antenna geometry (planar and circular) is explained. In the literature review section, published research related to the implementation of the steepest descent algorithm, smart signal processing algorithm in adaptive array antenna, and phased array antenna were summarized. Ideas and understanding on the implementation of the adaptive antenna array can be realized in terms of its concept, operation, method of implementation, performance, limitations, and suggestions for improvement.

2.1.1 Adaptive Array Antenna for GS Tracking Control System

An electronically beam steering adaptive array antenna for a GS tracking system is introduced in this dissertation as an alternative replacement of the traditional mechanical steering GS antenna system. This research is focusing on the development of the LMS algorithm in AAA for the GS tracking control system application. The AAA system is designed to be adapted with the signal environment, tailoring itself to the signal environment and exploit or reject the reflected signal. The architecture of a AAA is generally consisting of numbers antenna elements in an array configuration where each of the antenna elements is equipped with its own RF chain (receiver system) and its own analog/digital (A/D) converter [2] and phase shifter. The isolation of the incoming signals from multiple CubeSats, tracking the targeted CubeSat and suppress the interference from the interferer CubeSats can be achieved by performing the signal processing in the digital domain. The summary of the differences between phased array antenna (PAA) and adaptive array antenna (AAA) are as in Table 1.

Table 1: Differences between phased array antenna and adaptive antenna array

Descriptions	**Phased Array Antenna**	**Adaptive Antenna Array**
System Architecture	Combination of array antenna elements with phase shifters	Combination of PAA + DSP processor
Phase/Amplitude Signal Control	Phase/amplitude of received signal is fixed for each antenna element; usage of phase shifters	Phase/amplitude received signal is calculated by DSP processor (adaptively), based on the magnitude of the phase shifters
Radiation Signal Characteristics	Signal will be radiated in all directions at fixed amplitude gain beam (e.g: Switch Beam System)	Signal radiated only in the desired direction depends on where the users are
Interference Effect	Effect of the other interferences is neglected	Effect of other interferences are minimized

2.1.1.1 LMS Beamforming Architecture

Widrow and Hoff introduced the LMS algorithm in 1959, which uses a gradient-based method of steepest descent to minimize the MSE between the desired signal and the array output signal [3]. The LMS algorithm was adapted in the AAA control system because of its simplicity, ease of computation (does not need memory and matrix inversion) [4]. It was found to be the best choice for different adaptive signal processing [5]. Not limited to demonstrate the capability of self-steering beamforming and to minimize the MSE of the error signal, the LMS algorithm was implemented in the AAA system to provide the best possible estimation with each iteration until the weight has adapted or converged. An optimum set of weighting factors is determined to maximize the power of the desired signal or Signal-of-Interest (SOI) while minimizing the noise and interference or Signal-of-Not-Interest (SNOI). The performance of the LMS algorithm was verified by employing simulation in MATLAB software.

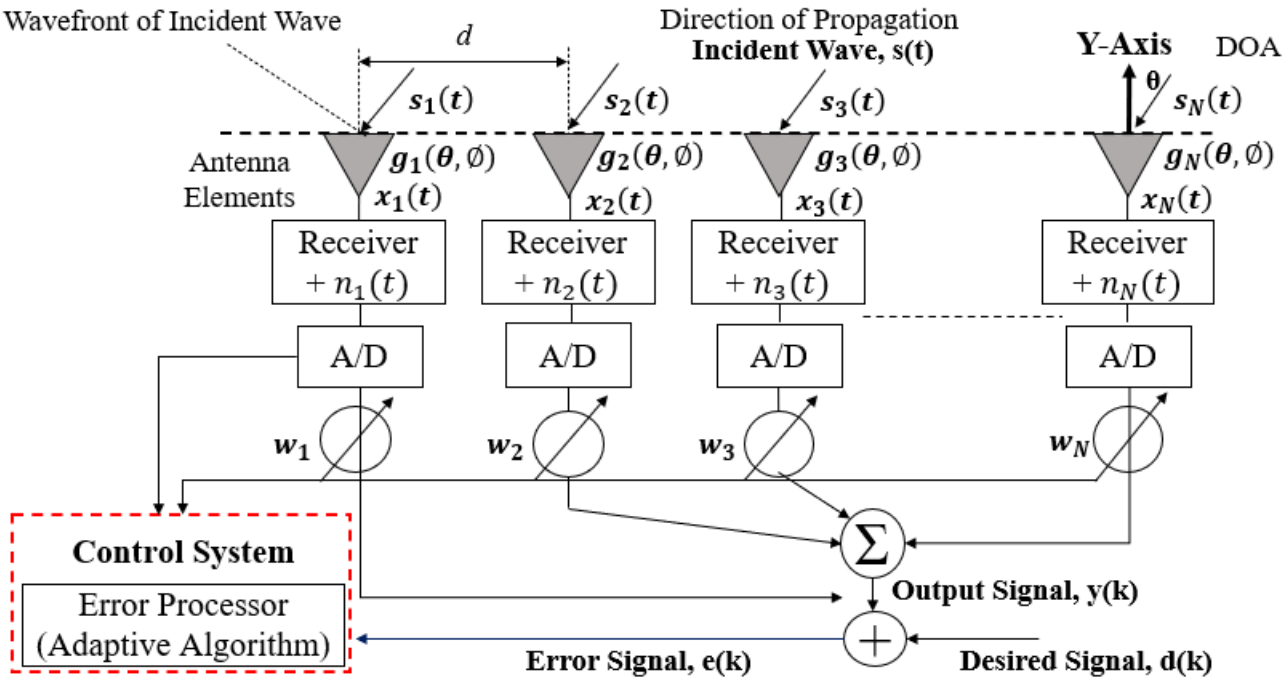

Figure 1: LMS beamforming network architecture [6], [7]

Generally, in the design of array architecture, the overall array radiation pattern is obtained from the radiation pattern of individual elements (include gain, $g_N(\theta,\emptyset)$), their positions, orientation in space, relative amplitude and phase of feeding currents to the elements. Steerable direction capability (without physically move any of individual elements) towards the desired user is achievable by varying amplitude and phase of individual elements output before the combining process. Fig. 1 shows the diagram of adaptive array architecture which is based on the LMS algorithm. Due to the difference in distance traveled by the wave between two antenna elements, the signals incident on all the antenna elements are in different phases. The signal present at Element #1 has traveled more distance $dsin(\theta)$ than signal present at Element #2, affected the phase of Element #1 lags Element #2 by $\beta dsin(\theta)$.

Where;

d: Distance between successive antenna phase centers in the array

β: Phase propagation factor $= 2\pi/\lambda$

λ: Wavelength of received signal

As the incident waves, $\mathbf{s}(t)$ arriving at antenna elements; electrical signals (incoming signals), $\mathbf{x}(t)$ is then down-converted by the receiver from Carrier Frequency, f_c to an Intermediate Frequency (IF). The IF is sampled by an Analog to Digital (A/D) converter to convert the electrical signals (incoming signals), $\mathbf{x}(t)$ into input signals, $\mathbf{x}_i(t)$ from analog to digital form signal as the waves reach the antenna elements. By referring to the diagram in Fig. 1, input signals, $\mathbf{x}_i(t)$, defined as $x_1(t)$, $x_2(t)$,…… $x_N(t)$ are multiplied with input weight (adjustable weights), w_1, w_2,…… w_N. The modification of amplitude and phase is applied during the multiplication process of each antenna element input signals, $\mathbf{x}_i(t)$ with input weights, $\mathbf{w}_i$. All the symbols are summed to produce an output signal (received signal), $y(t)$. In mathematical form, the general equation of the adaptive beamforming process can be written as in Eq. (1) [6]-[8]:

$$y(t) = \sum_{i=1}^{N} \mathbf{x}_i(t)\mathbf{w}_i. \quad (1)$$

Where;

$y(t)$: Output signal

N: Number of antenna elements

$\mathbf{x}_i(t)$: Input signals

$\mathbf{w}_i$: Input weights

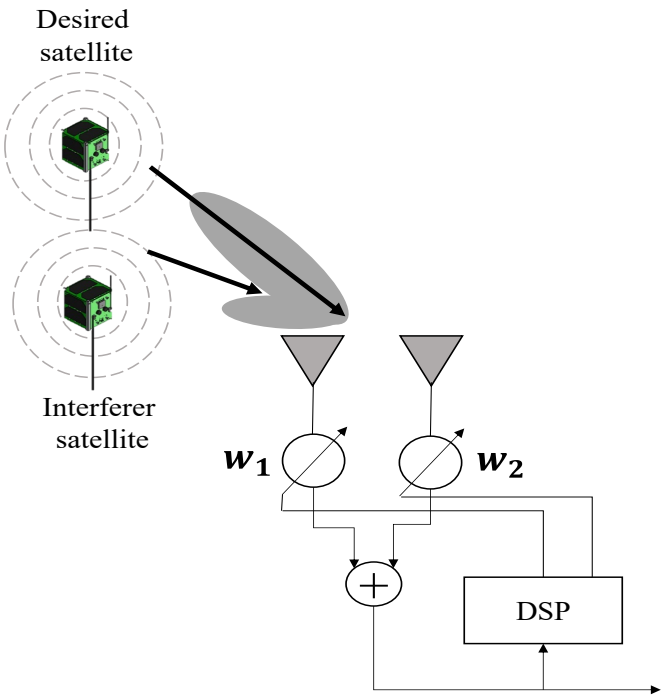

Figure 2: Adaptive antenna array [14].

LMS algorithm is an adaptive beam-forming algorithm for tuning the required signal and rejecting the interfering signal at the antenna array as illustrated in Figure 2. It is one of the most popular adaptive algorithms in the Temporal-Reference algorithm (one type of beamforming technique algorithm).

Consider that, i elements with $\mathbf{s}_i(t)$ signal sources present in the scenario. Based on the Temporal-Reference algorithm, a known reference signal (desired signal), $d(t)$ is required to be included in the frame of the signal, in the presence of more sources (signals from other satellites). In this AAA case, $d(t)$ is the signal from the tracked CubeSat. Assumed that, the satellite trajectory is known with a valid hypothesis if the orbit propagators are used to generate the satellite trajectory. In this case, Two Lines Element (TLE) is used. Aims of using beamforming technique algorithm are to minimize the energy of an error signal integrated by interferences and noises. Iterative procedure for weight calculation leads to MSE, mathematically can be calculated as [4]:

$$y(t) = \sum \mathbf{s}_i(t)\mathbf{a}(\theta)' + \sum \mathbf{I}_i(t)\mathbf{a}(\theta)'' + \mathbf{n}(t). \quad (2)$$

Where;

i: Number for each array antenna element from 1 to N

N: Total number of an array antenna element

$y(t)$: Antenna array output

$\mathbf{s}_i(t)$: The received signal from a CubeSat

$\mathbf{a}(\theta)'$: Steering vector for the desired direction

$\mathbf{I}_i(t)$: Interference signal

$\mathbf{a}(\theta)''$: Steering vector for undesired direction

$\mathbf{n}(t)$: Noise signal in the receiver channel connected to each antenna element (Gaussian noise with zero mean)

Noise is modeled by $\mathbf{n}(t) = [n_1(t)n_2(t) \ldots . n_N(t)]$, a $1 \times N$ row vector of complex white noise with variance, σ^2. The assumption is that each of the transmitted signals and noise sequences is mutually uncorrelated. The error processor computes the required weight adjustment to null out the undesired signal by iterative process and will continue until all the weights in the array converge. The adaptive algorithm is exploited to minimize the error signal, $e(t)$ between the reference signal (desired signal), $d(t)$ and the received signal, $y(t)$ which can be written as in Eq. (3):

$$e(t) = d(t) - y(t). \quad (3)$$

A narrow band incident wave (received signal), $\mathbf{s}(t)$ which arrives at antenna elements is written as in Eq. (4):

$$\mathbf{s}(t) = Aexp(2\pi f_c t + \emptyset). \tag{4}$$

Where;

A: Amplitude of the received signal

f_c: Carrier Frequency

$\emptyset$: Phase difference between incident waves at successive elements $= 2\pi/\lambda dsin(\theta)$

By taking received signal at Element #1 as the reference, the received signals, $\mathbf{x}_i(t)$ for uniform linear array with element spacing, d is represented in matrix form as in Eq. (5) [8]:

$$\mathbf{x}_i(t) = \begin{bmatrix} 1 \\ exp[-j\beta dsin(\theta)] \\ \vdots \\ exp[-j\beta(N-1)dsin(\theta)] \end{bmatrix} \mathbf{s}(t), \tag{5}$$

which can be simplified as Eq. (6)

$$\mathbf{x}_i(t) = \mathbf{a}(\theta)\mathbf{s}(t). \tag{6}$$

Where;

N: Number of antenna elements

θ: Angle of arrival with respect to Y-axis

$\mathbf{a}(\theta)$: Steering vector which control the direction of antenna beam at angle-of-arrival, θ

By inserting Eq. (5) into Eq. (1), yield Eq. (7)

$$y(t) = [w_1, w_2, \dots w_N] \begin{bmatrix} 1 \\ exp[-j\beta dsin(\theta)] \\ \vdots \\ exp[-j\beta(N-1)dsin(\theta)] \end{bmatrix} \mathbf{s}(t) \tag{7}$$

which can be simplified as in Eq. (8)

$$y(t) = \mathbf{w}_i \mathbf{x}^T(t). \tag{8}$$

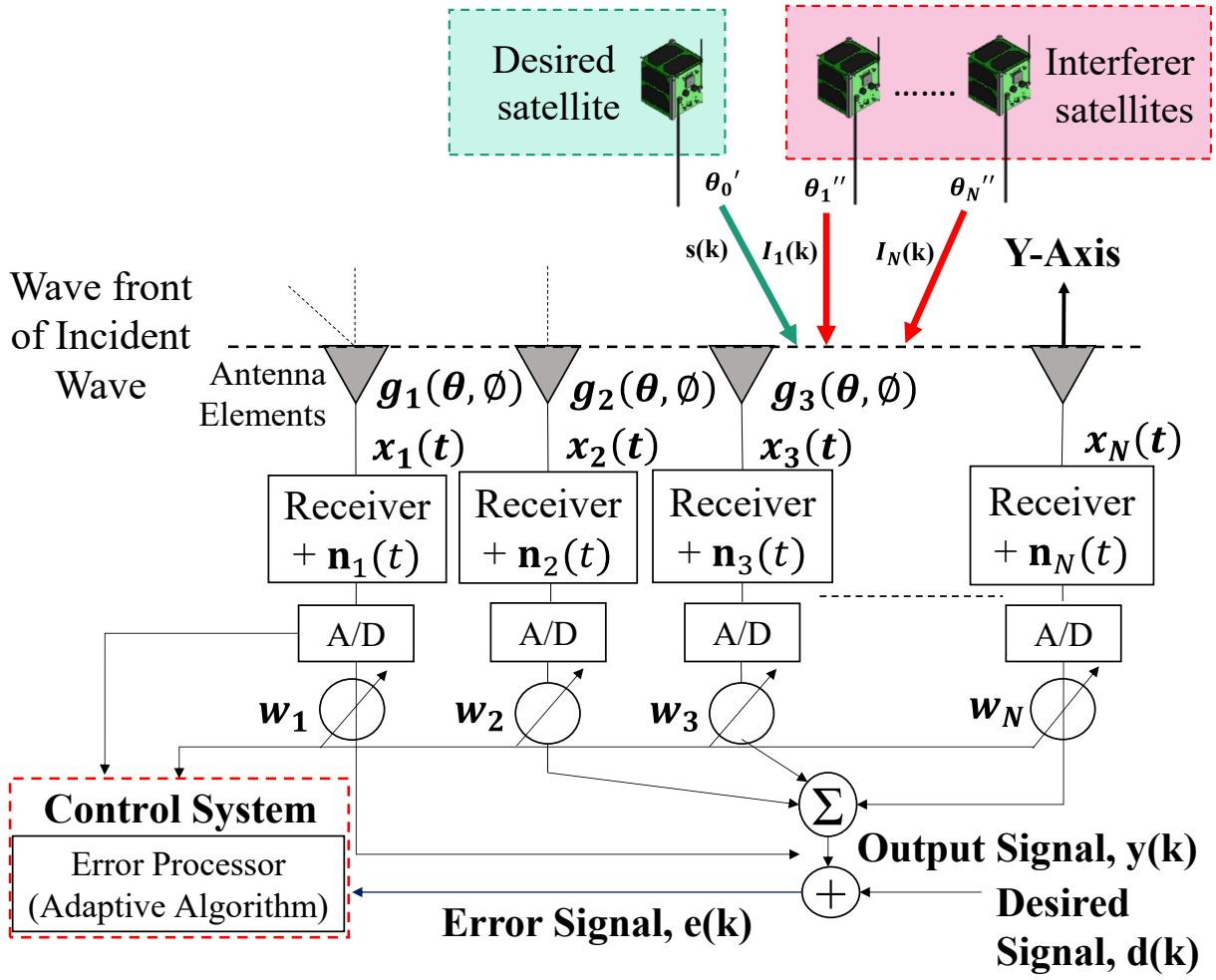

Figure 3: Beamformer array [6], [7]

The overall antenna pattern is continuously modified by adjusting the weight vector. For the digital communication system, the input signals are in a discrete-time sampled-data form. Therefore, the weighted output signal will be as in Eq. (9):

$$y(k) = \mathbf{w}(k)\mathbf{x}^T(k). \tag{9}$$

Where;

k: k^{th} sampling instant

Instantaneous value of the total received signal vector, $\mathbf{x}^T(k)$;

$$\mathbf{x}^T(k) = \mathbf{a}(\theta_0)'\mathbf{s}(k) + [\mathbf{a}(\theta_1)''\mathbf{a}(\theta_2)'' \ldots\ldots \mathbf{a}(\theta_N)''] \cdot \begin{bmatrix} \mathbf{I}_1(k) \\ \mathbf{I}_2(k) \\ \vdots \\ \mathbf{I}_N(k) \end{bmatrix} + \mathbf{n}(\mathrm{k})$$

$\mathbf{x}^T(k) = \mathbf{x}_s(k) + \mathbf{x}_I(k) + \mathbf{n}(k)$

From Eq. (9), $y(k) = \mathbf{w}(k) \cdot [\mathbf{x}_s(k) + \mathbf{x}_I(k) + \mathbf{n}(k)]$ or $\mathbf{w}(k) \cdot [\mathbf{x}_s(k) + \mathbf{u}(k)]$

Where;

$\mathbf{u}(k) = \mathbf{x}_I(k) + \mathbf{n}(k)$ is the undesired signal

The weighted array output power for the **desired signal** is given by:

$\sigma_s{}^2 = E[|\mathbf{w}(k) \cdot \mathbf{x}_s|^2] = \mathbf{w}(k) \cdot R_{ss} \cdot \mathbf{w}_k$

Where;

R_{ss} is the signal correlation matrix, given by:

$R_{ss} = \mathrm{E}[\mathbf{x}_s \mathbf{x}_s{}^H]$

The weighted array output power for **undesired signal** is given by:

$\sigma_u{}^2 = E[|\mathbf{w}(k) \cdot \mathbf{u}|^2] = \mathbf{w}(k) \cdot R_{uu} \cdot \mathbf{w}_k$

Where;

$R_{uu} = R_{II} + R_{nn}$

Where;

R_{II} is the correlation matrix for interferers

R_{nn} is the correlation matrix for noise

2.1.1.2 Weight Calculation from the Steepest Descent Method

Steepest Descent method based on gradient-based is implemented in the LMS algorithm to update weights, avoid the direct matrix inversion and minimize the MSE. The basic description of the LMS algorithm is as in Eqs. (10) and (11) [6]:

$$e(k) = d(k) - \mathbf{w}(k)\mathbf{x}^T(k). \quad (10)$$

$$\mathbf{w}(k+1) = \mathbf{w}(k) - \mu\nabla\xi(k). \quad (11)$$

Where;

$e(k)$: Error signal between the reference signal and the output signal (applied in case of SOI and SNOIs)

$\mathbf{w}(k)$: Value of weight vector before adaptation at a time, k

$\mathbf{w}(k+1)$: Value of weight vector after adaptation (updated weight) at a time, k

μ: Step-size which controls the speed of convergence

$\nabla\xi(k)$: A gradient of the cost function

which

$$\xi(k) = E[e^2(k)], \tag{12}$$

where

E is the expectation error signal (unknown), and therefore instantaneous value is used as an estimation. Therefore, Eq. (12) becomes Eq. (13):

$$\xi(k) = [e^2(k)], \tag{13}$$

where

$e^2(k)$ is the MSE between beamforming output signal, $y(k)$ and the reference signal, $d(k)$. By referring to Eq. (12), the derivation of the gradient of cost function, $\nabla\xi(k)$ becomes as in Eq. (14):

$$\nabla\xi(k) = -2e(k)\mathbf{x}(k), \tag{14}$$

by substituting the Eq. (14) into the general equation of the Steepest Descent algorithm in Eq. (11), yield Eq. (15):

$$\mathbf{w}(k+1) = \mathbf{w}(k) + 2\mu e(k)\mathbf{x}(k). \tag{15}$$

The tap weight of the vector is updated in preparation for the new sample/next iteration by the Eq. (15); where $\mathbf{w}(k)$ is the weight vector before adaptation at a time, k, while $\mathbf{w}(k+1)$ is the weight vector after adaptation at a time, k. μ is the step-size or gain constant which controls the convergence characteristics of the LMS algorithm. The LMS algorithm is initiated with some initial weights, to converge and stay stable, the μ value should be within the limit of $0 < \mu < \frac{1}{\lambda_{max}}$, where λ_{max} is the maximum Eigenvalue of the input covariance matrix. According to (Breslin, 1997) in [8], if μ is chosen to be a very small value, then the algorithm converges very slowly. Otherwise, a large value of μ may lead to a faster convergence but may be less stable around the minimum value [6]. The proper technique of choosing the μ value is by firstly use the maximum allowed value, and once the change in error is stabilized, the μ is reduced to reach the best result. $e(k)$ is known as the error estimation and $\mathbf{x}(k)$ is the input vector of time-delayed input values.

2.1.2 Array Factor

Array factor (AF) indicates the strength of the signal coming from a given direction. AF is calculated as a function of weights, positions and steering vector applied in the phased array antenna. The AF quantifies the effect of combining radiating elements in an array without considering the element-specific radiation pattern. It is based on interference between the radiated

fields of the elements in the array. The manipulation of the weights allows the AF to be tailored to the desired array patterns. The response of AF is strongly influenced by individual type of geometry array; in this research, planar and circular array geometry are considered. In the case of adaptive array antennas, the position of the antenna elements should be kept fixed. Only optimal weights are considered for optimal radiation pattern, which shows good null depth along the undesired direction and satisfied the AF gain along the main lobe (desired direction). Detailed analysis of the beam pattern characteristics, array size, antenna element distribution are carried out and discussed further in Chapter 4.

2.1.2.1 Planar Array Geometry

Planar array antenna (considering $M \times N$ isotropic elements) geometry is commonly used in AAA as it has the capability of steering/scanning the main beam towards any desired direction (at maximum radiation and reception in both azimuth, $\emptyset$ and elevation, θ) [9]. Moreover, a planar array antenna is more versatile as it provides more symmetrical patterns with lower side lobes, much higher directivity (narrow main beam). Based on planar array factor geometry in Fig. 4, the general equation of planar array factor is as calculated in (16):

$$AF = AF_x AF_y$$

$$= \sum_{m=1}^{M} \sum_{n=1}^{N} \mathbf{w}_{mn} e^{j[(m-1)(\Psi_x+\beta_x)+(n-1)(\Psi_y+\beta_y)]}. \quad (16)$$

Where;

$\mathbf{w}_{mn}$ = Complex array weight at element m, n

$\Psi_x = kd_x sin_\theta cos_\emptyset$

$\Psi_y = kd_y sin_\theta sin_\emptyset$

$\beta_x = -kd_x sin_\theta cos_\emptyset$

$\beta_y = -kd_y sin_\theta sin_\emptyset$

Where;

k = Wave number ($2\pi/\lambda$)

d_x, d_y = Inter-element spacing for x, y

θ = Angle of incidence of an electromagnetic plane wave from array axis

$\emptyset$ = Angular position of m^{th}, n^{th} elements on x, y plane

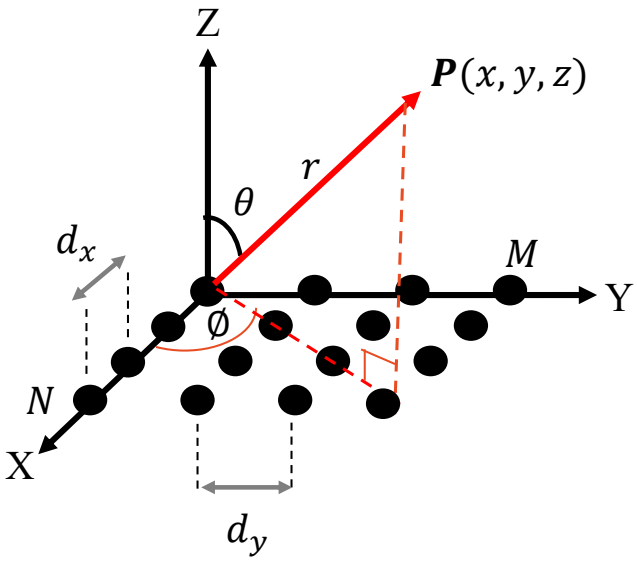

Figure 4: Planar array geometry

2.1.2.2 Circular Array Geometry

On the other hand, circular array can scan in either azimuth or elevation directions and have uniform resolution over the azimuth (without significant change in beam shape) but nonuniform resolution over the elevation. Since it does not have an edge element and edge constraints, the beam pattern of circular array can be electronically, rotated. Furthermore, it has the capability to compensate the effect of mutual coupling by breaking down the array excitation into a series of symmetrical components. However, there will be space limitations in the real implementation. Consider a Uniform Circular Array (UCA) with N antenna elements positioned equidistant from each other and at radius, r from the centre of an array. The circular array geometry is as shown in Fig. 5. General equation of circular array factor is as calculated in (17):

$$AF(\theta, \emptyset) = \sum_{n=1}^{N} \mathbf{w}_n e^{-jka[sin(\theta)cos(\emptyset-\emptyset_n)-sin(\theta)cos(\emptyset_0-\emptyset_n)]} \quad (17)$$

Where;

$\mathbf{w}_n$ = Excitation coefficients (amplitude and phase) of n^{th}

$\emptyset_n = 2\pi(n/N)$ = Angular position of n^{th} element on x, y plane

k = Wave number ($2\pi/\lambda$)

θ = Angle of incidence of electromagnetic plane wave from array axis

$\emptyset$ =Angular position of m^{th}, n^{th} elements on x, y plane

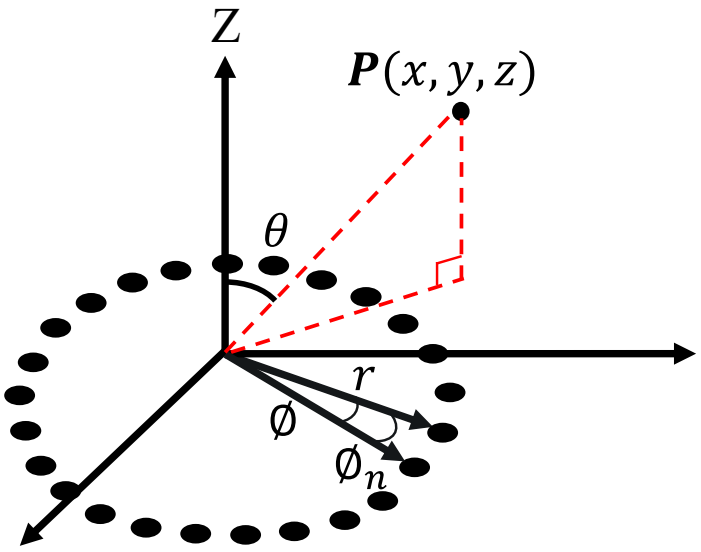

Figure 5: Circular array geometry

2.2 Literature Review

There are many other existing kinds of research regarding the implementation of the steepest descent algorithm / smart signal processing algorithm in the adaptive array antenna/phased array antenna for on-board satellite applications that have been proposed. However, until now, there is still a lack of literature reviews mentioning about the implementation of the AAA control system at the ground station side. In this section, some of the relevant literature reviews are discussed as follows.

2.2.1 Modelling and Simulation of Phased Array Antenna for LEO Satellite Tracking

Kyun, N. C. et al. (2002) introduced a sophisticated phased array antenna for LEO satellite tracking in [10] since the LEO satellite systems revolving around the Earth overlay mobile terminals (MT) or Earth stations over only several minutes. They claimed that although phased array antenna has been widely used for mobile cellular communication systems with advantages of its electronic beam steering, it is still not truly used in integrate with LEO Mobile Satellite System (MSS). A substantial part of this paper presented a MATLAB simulation results and analysis of the design of the phased array antenna mathematical models for LEO satellite tracking applications. The presented simulation results are beam steering, beam width and multiple beams

of the phased array antenna. In the beam steering phased array antenna results, researchers found out that, when the phase shifter is turned to - 180º, the main lobe directivity will steer to 0º from the phased array antenna with high gain while other sidelobes level are low. They explained that the 0º directivity beam phenomenon is known as end-fire steering. It is impossible to perform a satellite tracking even when the satellite position is below the 8.2º elevation angle. Detail discussion on the issues related is discussed further. Further analysis of the number of antennas' parameters and an overview of the satellite constellation systems' characteristics were also described in [10]. The simulation of beamforming using a phased array antenna is explored to obtain multiple and steerable beams for tracking the satellite smoothly. Finally, an integration of a phased array antenna in MT is proposed for future global wireless communication systems.

2.2.2 Performance Analysis of Least Mean Square Sample Matrix Inversion Algorithm for Smart Antenna System

Ali, W. A. et al. (2013) in [4] proposed a hybrid algorithm that is a combination of two algorithms, the Least Mean Square (LMS) algorithm and Sample Matrix Inversion (SMI) algorithm as the beamforming technique. The common disadvantage of the LMS algorithm is slow convergence rate because the initialization of the weights was performed, arbitrarily. However, the authors introduced a hybrid algorithm LMS/SMI to an array of dipoles to overcome the demerits of the LMS algorithm for a robust smart antenna system. The weights of the inversion matrix in SMI were calculated and these weights will be the initial weights in the LMS algorithm, instead of arbitrarily weights. Consequently, the main beam of the antenna will be steered, focusing on the desired direction and place null in the direction of interference signals. The findings of this paper are solving the LMS slow convergence rate problem and the computation-intensive exists in the SMI algorithm, as well as decreases the LMS error. The simulation results indicate the analyses of LMS, SMI and hybrid algorithm performances. These techniques are compared and verified using MATLAB. From the study, authors found out that although the SMI can track the actual signal faster than LMS, LMS tracks the actual signal more accurate. They concluded that the hybrid algorithm LMS/SMI provides better performance rather than LMS and SMI.

2.2.3 Adaptive Antenna Arrays for Satellite Personal Communication Systems

Lian, K. J. (1997) in her thesis [7] discussed the motivation of personal communication services implemented employing multiple satellite systems. She explained theoretically on geometrical analysis in the literature review section. Several satellites constellations system was proposed in this paper to show how the number of satellites and orbits are estimated. The network management issues experienced by different constellations are described in the paper. Highlighted issues are related to antenna beams (such as multi-beam coverage and inter-satellite links), Doppler shift effect, co-channel interference and link budget analysis (rain attenuation, the effective isotopically radiated power (EIRP)), receiving and transmitting antenna gain and frequency). Lian proposed adaptive antenna arrays mounted on the handheld terminals to overcome these issues. This technique is believed to be better than omnidirectional antennas which radiate in all directions because of the adaptation to the changing environment, ability to reject interference and track the satellite automatically. The LMS algorithm was investigated and used in the simulation of the adaptive array. She advised applying antenna element spacing of 0.5λ to 0.8λ to avoid the appearance of grating lobes in the antenna pattern. This condition is only applicable to the linear and planar equally spaced array antenna. The effect of the appearance of grating nulls that cause the additional grating nulls to appear at the other angles is also discussed in [7]. An undesirable low Signal-to-Interference-plus-Noise Ratio (SINR) results are expected if the desired signals fall in a grating null. The overall performance of the LMS array was discussed in detail.

2.2.4 Adaptive Array Antennas for Mobile Earth Stations: A Review

Alio, S. and Kudsi, L. (2017) wrote a review in [11] about adaptive array antennas for mobile earth stations. They highlighted the effect of the interference and the multi-path fading, which contributes to significant problems for receiving a dependable signal and leads to significant degradation performance. A solution to mitigate this problem was proposed in [11], which utilizes antenna array systems on mobile user terminals. These systems will steer the radiation pattern towards the satellite signal and dynamically put nulls in the direction of the interference and the multi-path signals. This will be done in real-time using smart signal processing algorithms, which are the critical elements of the adaptive array antenna systems. These algorithms were used to determine spatial signal parameters such as direction-of-arrivals (DOAs) of incoming signals, form the beams, and steer them in the desired directions while minimizing the interference. The authors

proposed several algorithms to perform specific tasks. Multiple Signal Classification (MUSIC) and Estimation of Signal Parameter via Rotational Invariance Techniques (ESPRIT) algorithms were used to estimate the DOA signal. LMS and Recursive-Least-Squares (RLS) algorithms used for beam pattern steering towards the desired direction and putting null towards the undesired signal. Finally, the authors suggested the possibility of implementing an adaptive antenna array onboard a satellite.

2.2.5 New Receiving Ground Antenna using Active Phased Array Antenna for Satellites

Kaya, N. and Mankins, J. (2016) discussed in [12] the development of a ground receiving station using an active phased array antenna. The authors focused on building the active phased array antenna with hundreds of poles circularly aligned antenna elements which receives X-band signal from the LEO nanosatellites. The target frequency is X-band for the communication between the nanosatellites and the ground receiving stations. Further link budget calculation was performed to estimate the X-band signal transmitted from satellite. The authors presented the block diagram of the proposed ground station system and its architecture. The system consists of an omnidirectional antenna, amplifier, phase shifter, frequency mixer, and the power combiner by using the computer. The 8-array antenna experiment was performed to investigate its reception results, where the system control beam directions electronically, by the computer.

CHAPTER 3

RESEARCH METHODOLOGY

3.1 Overview

This chapter explains the research methodology that involves the MATLAB simulation of the LMS algorithm. There are five stages to fulfill this research which involve the literature review, determination of massive CubeSats constellations and creating three real-time scenarios in STK, simulating orbital analysis in STK and obtaining the AER data from the STK Report Access, preparing LMS algorithm and test its performance by analyzing the main beampattern behavior and the Signal-to-Interference Ratio (SIR) and finally, investigate the capability of the algorithm to perform fast-tracking with the optimum beam pattern. The literature review part in Chapter 2 is essential for determining the research topic and identifying the research gap and novelty. Various works have been published and recent works suggested a new technique of AAA which is possible to be implemented in the GS tracking system. The general knowledge and proposed ideas of the AAA, smart antenna system and development of LMS algorithm in the aspect of basic theory, the principle of operation, structure limitations and performance were discussed in the literature review.

3.2 Design Process

Details of the design process of the adaptive array antenna using LMS algorithm can be simplified into a few steps as listed below:

1. Antenna geometry selection: The suitable antenna geometry for satellite communication is identified.
2. Number of antenna elements: Starts simulation with a small number of antennas. In this research, 64 number of antenna elements was chosen as a starter.
3. Array antenna design: Involving the fixed selection of antenna geometry, inter-element spacing, d, and finally number of antenna elements.
4. Signal processing algorithm selection: LMS algorithm is selected to minimize the Mean Square Error (MSE) and perform sidelobes reduction.
5. Design optimization: Optimization of array beam pattern can be done by optimizing the input parameters in the LMS algorithm.

6. LMS calculation and weights updated: Scanning the main beam pattern towards the Signal-of-Interest (SOI) while placing null towards Signal-Not-of-Interest (SNOI).
7. Array Factor (AF) analysis: Compare the Array Factor (AF) results produced by LMS weights and analyze the amplitude of the main beam pattern with the presence of the other sidelobes. Signal-to-Interference Ratio (SIR) can be calculated with the AF plots.
8. Optimal set of weighting factors computed by LMS: Provide a narrow beam width beam pattern, high SIR, suppressed sidelobes and compute the best weight estimation until converged.
9. Analysis of the LMS performance for massive CubeSats constellations: Involving the real scenarios of LEO massive CubeSats constellations.
10. LMS overall performance verification: Verify the LMS overall performance by analyzing SIR and CPU time results.

3.3 Flow Chart

The overall work is shown as a flow chart in Figure 6.

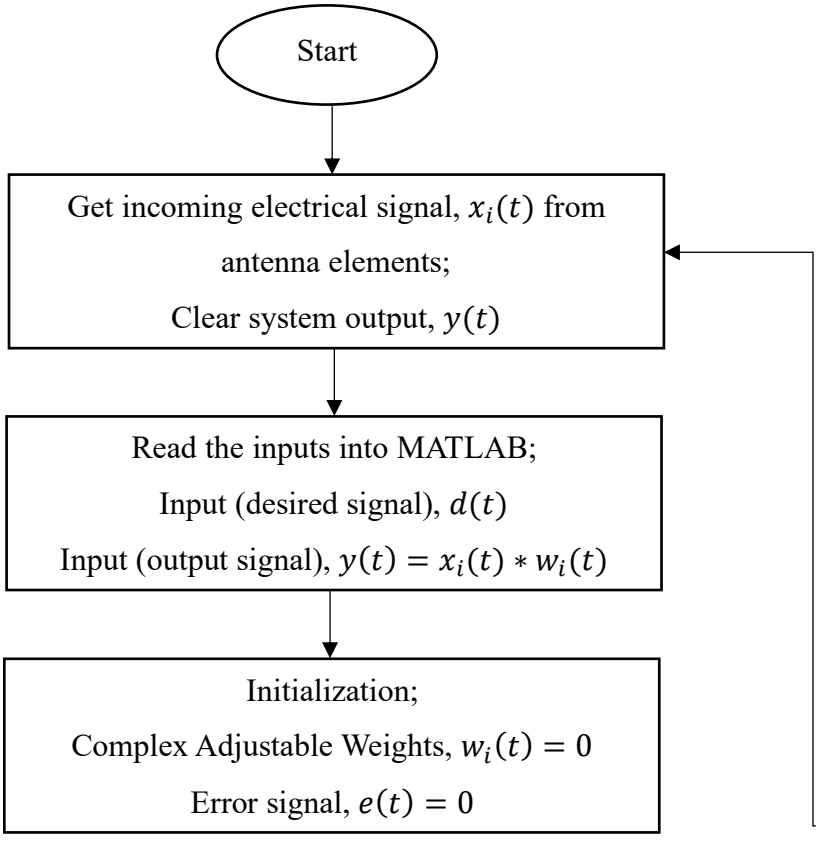

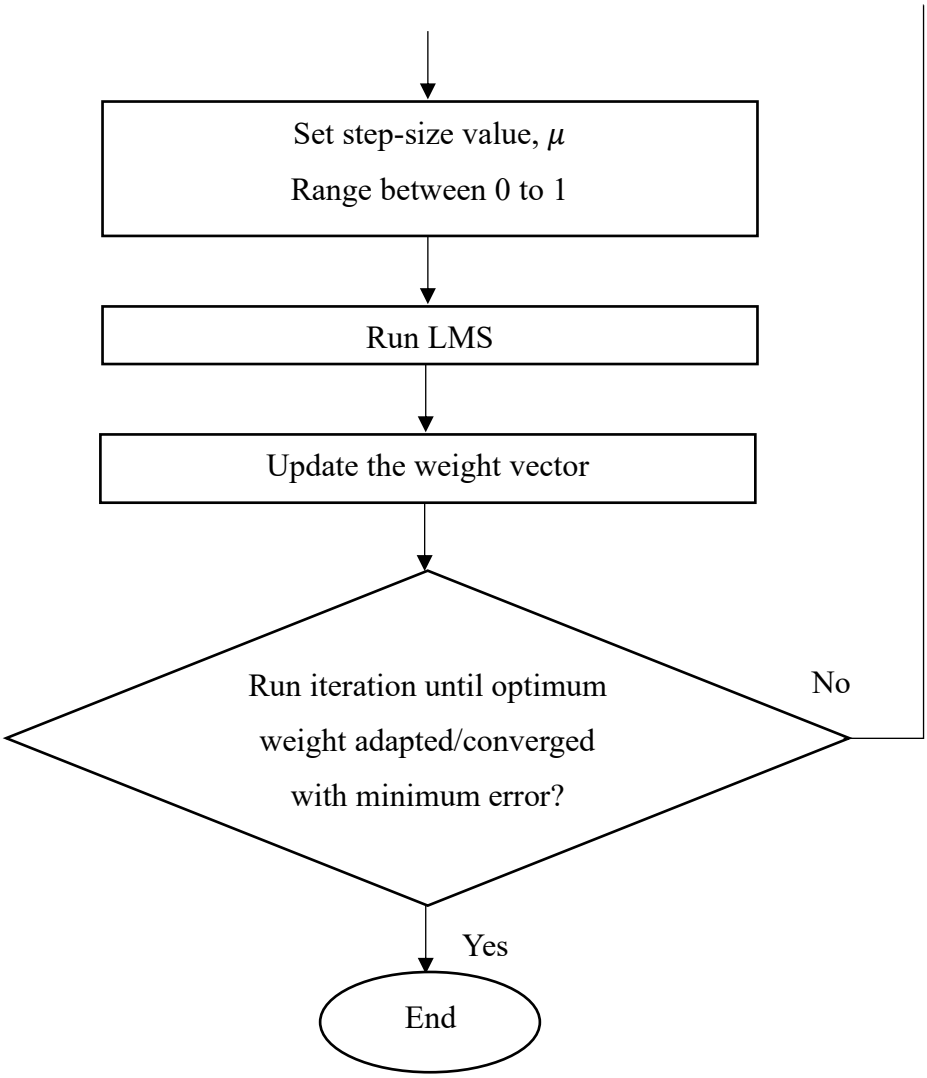

Figure 6: LMS algorithm flow chart

3.4 Orbital Analysis for Massive Constellation

The real-time orbital analysis of LEO CubeSats constellations was simulated in STK software. The Two-Line Element (TLE) orbital information (CubeSat's location and pointing angles at any point in time) was imported from the public online satellite databases [13]. Three scenarios under analysis were created for CubeSats constellations launched within January 12th to June 29th, 2018 involving two units of 1U BIRDS CubeSats constellation from BIRDS-2 Project, ten units of 3U FLOCK-4A and eight-unit of FLOCK-3P CubeSats constellation from Planet Lab and eleven units of 3U LEMUR-2 CubeSats from Spire Global, Inc. The orbital analysis was performed from the point of view of BIRDS GS at Kyushu Institute of Technology (Kyutech),

Japan from May 14th, 2019 (00:00:00 UTC) until May 15th, 2019 (00:00:00 UTC). BIRDS GS is located at 33.52° N and 130.50° E with antenna boresight direction pointing to the BIRDS-2, FLOCK-4A and LEMUR-2 CubeSats. From the analysis, three different scenarios of constellations are created in STK, considering CubeSats constellations on the same or different orbital planes. Constellation 1: Involving BIRDS-2 and Planet Labs CubeSats in different orbital plane and different orbital inclination, having a number of CubeSats, $N_S = 11$, located on two different orbital planes and two different inclination over the equatorial plane. Constellation 2: Involving Spire Global Inc. CubeSats, having a number of CubeSats, $N_S = 11$, located on the same altitude but different in the orbital inclination over the equatorial plane. Constellation 3: Involving Planet Labs and Spire Global Inc. CubeSats, having a number of CubeSats, $N_S = 12$, located on a different altitude, orbital inclination and plane over the equatorial plane.

3.5 CubeSats Constellation Scenario Under Analysis

According to the Report Access: AER (Azimuth (º), Elevation (º) and Range (km)) generated in the STK orbital simulation, precise locations of CubeSats under analysis are determined. By referring to the planar and circular array geometry in Fig. 2 and Fig. 3, the phi, $\emptyset$ represents the azimuth (degree), the theta, θ represents the elevation (degree) and R represents the range (km) from the observation point, P. Objects (CubeSats Under Analysis) are accessed from the Kyutech GS. The generated Report Access analysis for Scenario 1, 2 and 3 are as in Table 2. Based on the information generated from the Report Access in Table 2, the AER data are used in the simulation of the LMS algorithm in MATLAB simulation software for interference analysis. The presence of interferers is evaluated by considering three beam patterns; main lobe (towards targeted CubeSat) and side lobes (towards interferer CubeSats). Table 3 summarizes the orbital planes involved in each scenario. The altitude, inclination and longitude of the ascending node of the CubeSats involved are listed in the table.

Table 2: Report Access: Azimuth, Elevation and Range (AER) of Scenario 1, 2 and 3 in STK

Scenario	CubeSats	AOS, Max El, LOS (UTC)	AER
1	FLOCK 4A-12	12:52:27	187,0,2600
		12:58:02	262,32,884
		13:03:37	337,0,2605
	FLOCK 4A-9	12:44:38	182,0,2601
		12:50:19	261,41,740
		12:56:00	340,0,2605
	MAYA-1	12:48:28	235,0,2249
		12:53:36	319,54,469
		12:58:48	43,0,2267
	FLOCK 4A-10	12:49:49	185,0,2601
		12:55:26	262,34,834
		13:01:04	338,0,2606
	FLOCK 4A-11	12:51:53	187,0,2601
		12:57:28	262,32,873
		13:03:04	338,0,2605
	UiTMSAT-1	12:55:10	238,0,2250
		13:00:17	320,44,532
		13:05:27	42,0,2268
	FLOCK 4A-5	12:53:12	188,0,2600
		12:58:46	262,31,899
		13:04:21	337,0,2605
	FLOCK 4A-6	12:55:16	189,0,2601
		13:00:48	262,29,940
		13:06:21	336,0,2605
	FLOCK 4A-7	12:56:49	190,0,2601
		13:02:19	263,28,971
		13:01:51	336,0,2606
	FLOCK 4A-8	12:57:30	190,0,2601
		13:02:59	263,27,985
		13:08:31	335,0,2605
	FLOCK 4A-15	12:44:38	182,0,2601
		12:50:18	261,41,740
		12:56:00	340,0,2605
	FLOCK 4A-16	12:46:20	183,0,2601
		12:52:00	261,39,770
		12:57:40	340,0,2606
2	LEMUR-2_XUENITERENCE	12:10:42	165,0,2564
		12:16:42	14,72,519
		12:22:11	350,0,2598
	LEMUR-2_NOGUECORREIG	12:06:31	139,0,2570
		12:11:31	72,21,1150
		12:17:01	6,0,2594

Scenario	CubeSats	AOS, Max El, LOS (UTC)	AER
	LEMUR-2_SPIREMINIONS	12:05:02	138,0,2570
		12:10:15	72,21,1150
		12:15:30	6,0,2594
	LEMUR-2_WINGO	12:10:05	283,0,2549
		12:14:17	237,7,1839
		12:18:28	191,0,2535
	LEMUR-2_ANDIS	12:18:13	64,0,2821
		12:20:38	87,2,2629
		12:23:03	110,0,2810
	LEMUR-2_GUSTAVO	13:51:26	36,0,2786
		13:56:26	90,13,1683
		14:01:46	150,0,2770
	LEMUR-2_URAMCHANSOL	13:47:16	38,0,2784
		13:52:21	93,12,1736
		13:57:24	148,0,2773
	LEMUR-2_PETERWEBSTER	12:06:51	134,0,2554
		12:11:54	71,18,1242
		12:16:59	7,0,2576
	LEMUR-2_ZO	13:41:10	42,0,2785
		13:46:10	96,9,1929
		13:50:34	142,0,2711
	LEMUR-2_YONGLIN	15:18:06	190,0,2394
		15:23:00	127,17,1185
		15:27:56	64,0,2410
	LEMUR-2_KADI	13:37:13	43,0,2783
		13:41:13	83,8,1996
		13:46:23	140,0,2773
3	LEMUR-2_NOGUECORREIG	12:06:31	138,0,2567
		12:11:45	72,22,1126
		12:17:01	5,0,2593
	LEMUR-2_SPIREMINIONS	12:05:03	138,0,2570
		12:10:11	72,21,1150
		12:15:30	6,0,2594
	LEMUR-2_PETERWEBSTER	12:06:51	135,0,2554
		12:11:54	71,18,1242
		12:16:59	7,0,2576
	FLOCK-3P-1	11:48:46	124,0,2564
		11:53:25	69,12,1556
		11:58:04	14,0,2585
	FLOCK-3P-4	11:41:39	118,0,2573
		11:46:04	68,10,1701
		11:50:29	17,0,2593
	FLOCK-3P-14	12:08:52	138,0,2562
		12:14:05	72,21,1133

Scenario	CubeSats	AOS, Max El, LOS (UTC)	AER
		12:19:19	5,0,2587
	FLOCK-3P-23	11:48:17	124,0,2572
		11:52:57	69,12,1549
		11:57:39	13,0,2594
	FLOCK-3P-46	12:04:40	136,0,2564
		12:09:48	71,19,1206
		12:14:58	7,0,2590
	FLOCK-3P-47	12:05:31	136,0,2564
		12:10:41	71,20,1186
		12:15:52	6,0,2589
	FLOCK-3P-48	12:09:07	139,0,2563
		12:14:20	72,22,1116
		12:19:37	5,0,2589
	FLOCK-3P-78	12:08:55	138,0,2566
		12:14:08	72,21,1135
		12:19:23	5,0,2590

Table 3: Orbital Planes of Scenario 1, 2 And 3

Scenario	Altitude (km)	Inclination (degree)	Longitude of ascending node	CubeSats
1	505.7	97.5	195.3	FLOCK 4A-12
	507.1	97.5	195.6	FLOCK 4A-9
	386.1	51.6	156.1	MAYA-1
	506.6	97.5	195.6	FLOCK 4A-10
	506.1	97.5	195.3	FLOCK 4A-11
	382.3	51.6	157.7	UiTMSAT-1
	505.9	97.5	195.6	FLOCK 4A-5
	506.1	97.5	195.3	FLOCK 4A-6
	506.6	97.5	195.9	FLOCK 4A-7
	506.8	97.5	195.6	FLOCK 4A-8
	507.7	97.5	195.9	FLOCK 4A-15
	507.5	97.5	195.6	FLOCK 4A-16
2	515.4	97.4	193.2	LEMUR-2_XUENITERENCE

	502.4	97.4	202.1	LEMUR-2_NOGUECORREIG
	504.1	97.4	202.0	LEMUR-2_SPIREMINIONS
	482.2	51.7	10.0	LEMUR-2_WINGO
	592.1	97.6	30.3	LEMUR-2_ANDIS
	575.9	97.7	43.9	LEMUR-2_GUSTAVO
	572.8	97.7	43.5	LEMUR-2_URAMCHANSOL
	498.4	97.5	203.2	LEMUR-2_PETERWEBSTER
	572.7	97.7	43.9	LEMUR-2_ZO LEMUR-2_YONGLIN
	432.5	51.6	216.9	LEMUR-2_KADI
	578.2	97.7	43.5	
3	497.4	97.4	202.1	LEMUR-2_NOGUECORREIG
	499.5	97.4	202.0	LEMUR-2_SPIREMINIONS
	507.1	97.5	203.2	LEMUR-2_PETERWEBSTER
	503.1	97.4	202.6	FLOCK-3P-1
	499.2	97.4	202.4	FLOCK-3P-4
	493.0	97.4	202.8	FLOCK-3P-14
	506.0	97.4	202.0	FLOCK-3P-23
	498.2	97.4	202.6	FLOCK-3P-46
	497.2	97.4	202.6	FLOCK-3P-47
	493.8	97.4	203.2	FLOCK-3P-48
	494.4	97.4	202.8	FLOCK-3P-78

3.5.1 Scenario 1

The first real-time scenario occurs on May 14th, 2019 at 12:57:57 UTC involving Constellation 1 where FLOCK 4A-12 CubeSat is the targeted CubeSat while 8 units of FLOCK 4A and 2 units of BIRDS-2 CubeSats (UiTMSAT-1 and MAYA-1) act as interferers. Fig. 7 shows the constellation 1 scenario: 3D orbital simulation of BIRDS-2 and Planet Labs CubeSats constellation on a different orbital plane and inclination simulated in STK software. The Acquisition of Signal (AOS) and Loss of Signal (LOS) of Constellation #1 passes are predicted by using Orbitron software, considering CubeSat elevation is 10^{o} and higher. The Constellation 1 sequence was started with the entry of FLOCK 4A-9 and FLOCK 4A-15 CubeSats into the Kyutech GS footprint and ended with FLOCK 4A-8 CubeSat. FLOCK 4A-12 CubeSat (the targeted CubeSat) entered the Kyutech GS footprint at AOS of 12:52:27 UTC and left the footprint at LOS of 13:03:37 UTC. This AOS and LOS time are chosen according to the prediction of FLOCK 4A-12 CubeSat at the maximum elevation angle of 32^{o} during the pass.

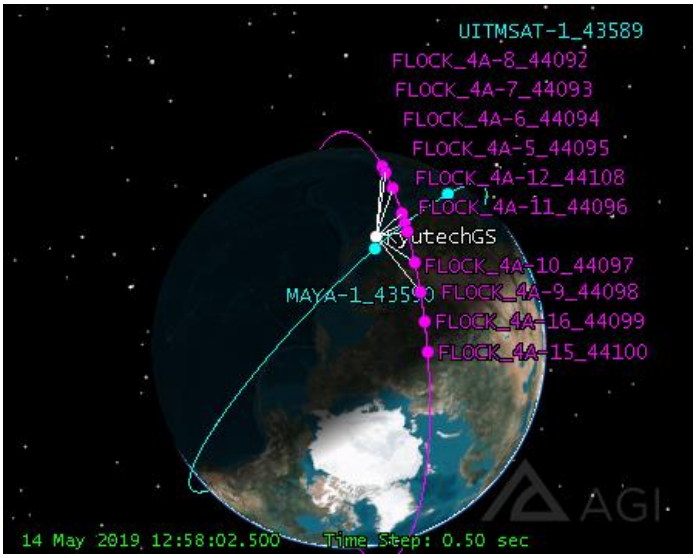

Figure 7: 3D orbital simulation of Scenario 1 in STK

3.5.2 Scenario 2

The second real-time scenario involves Constellation 2 which took place on May 14th, 2019 at 12:16:19 UTC involving LEMUR-2_XUENITERENCE CubeSat as the targeted CubeSat

while 10 units of other LEMUR-2 CubeSats act as interferers. Fig. 8 shows the Constellation 2 scenario: 3D orbital simulation of LEMUR-2 CubeSats constellation at the same altitude but in different orbital inclination simulated in STK software. LEMUR-2_SPIREMINIONS is estimated to be the first CubeSat passes the Kyutech GS, continued by LEMUR-2_NOGUECORREIG and LEMUR-2_WINGO. The AOS and LOS of the Constellation #2 are between 12:05:02 and 15:27:56 UTC with the sequence of CubeSat s started with LEMUR-2_SPIREMINIONS CubeSat and ended with LEMUR-2_YONGLIN CubeSat. The targeted CubeSat is LEMUR-2_XUENITERENCE at the maximum elevation angle of 72^{o} during the pass.

Figure 8: 3D orbital simulation of Scenario 2 in STK

3.5.3 Scenario 3

The third real-time scenario occurs on May 14th, 2019 at 12:11:41 UTC involving Constellation 3 where LEMUR-2_NOGUECORREIG CubeSat is the targeted CubeSat while the other 2 units of LEMUR-2 CubeSats and 8 units of FLOCK-3P CubeSats act as interferers. Fig. 9 shows the Constellation 3 scenario: 3D orbital simulation of FLOCK-3P and LEMUR-2 CubeSat constellation on different orbital planes simulated in STK software. For the third scenario, the sequence pass involving two different CubeSat s constellations on different altitude, inclinational and orbital plane. FLOCK-3P-4 is estimated to be the first CubeSat passes the Kyutech GS

footprint, continued by FLOCK-3P-23 and FLOCK-3P-1. LEMUR-2_NOGUECORREIG CubeSat (targeted CubeSat) entered the Kyutech GS footprint at AOS of 12:06:31 UTC and left the footprint at LOS of 12:17:01 UTC. This AOS and LOS time are chosen according to the prediction of LEMUR-2_NOGUECORREIG CubeSat at the maximum elevation angle of 22^{o} during the pass.

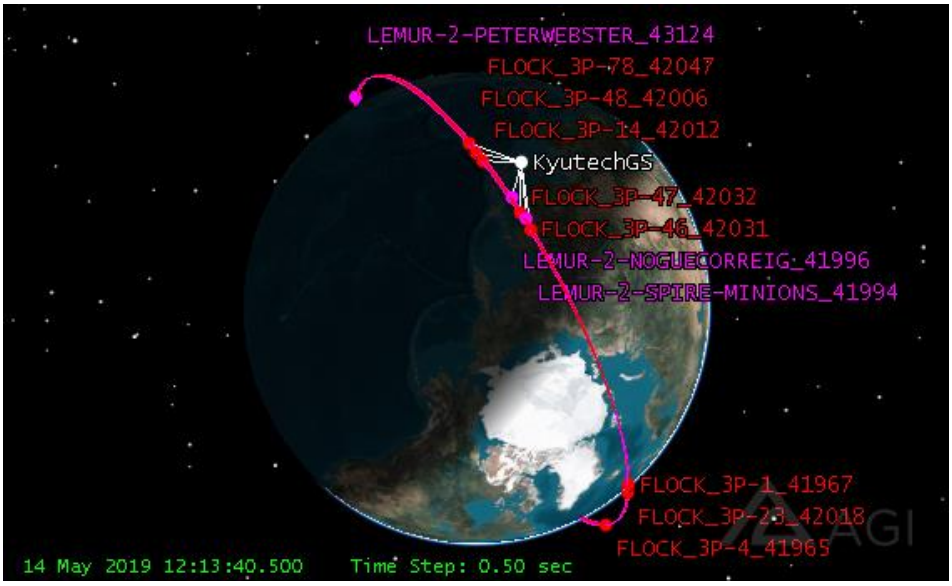

Figure 9: 3D orbital simulation of Scenario 3 in STK

CHAPTER 4

RESULTS AND DISCUSSION

4.1 Overview

This chapter discusses the results obtained from the MATLAB simulation of the LMS algorithm implemented in AAA for planar and circular array antenna geometry. The performance of the algorithm was measured by the SIR value, the beam width of the main beam pattern and the computational time (CPU time) for the algorithm to calculate weights. Parameters used as input obtain the optimum element weights where the optimum beampattern shapes were achieved. Detail explanation on how the step-size, mean, and variance of noise are determined, was explained in the results and analysis section.

4.2 Simulation Results and Analysis

The LMS simulation in MATLAB uses input parameters of targeted and interferes CubeSat's elevation and azimuth in Table 2, involving three scenarios of CubeSats constellations. The number of SOI (the targeted CubeSat) and SNOI (interferer CubeSats) are set as default parameters. To achieve a maximum ratio of desired signal strength to the interferer signal strength, 'Step-size value' ($Mu\ (\mu)$), 'Additive Noise' (Mean of Noise and Variance of the Noise) and 'Amplitude of SOI and SNOIs' are considered as input parameters for these three scenarios. These parameters are used as input to obtain optimum element weights, w_{opt}; where the optimum beam pattern shapes are achieved (the ratio of the main lobe to the side lobes of the beam pattern is high), the Mean Square Error (MSE) between the array output and the reference signal, $d(t)$is minimized and the SIR of the beam pattern is high. This does not always result in the beampattern having a maximum beam in the direction of the desired signal but does yield the array output signal with high SIR. Most often, this is accomplished by forming nulls in the directions of interfering signals. The step-size, μ is set to the value of 0.001, Mean of Noise and Variance of the Noise are set to 0 and 0.1, respectively. The step-size is chosen to be a small positive value when the algorithm is near the optimal solution to achieve a low level of misadjustment and thus achieving better overall performance. In practice, the input signal often contains white 'Gaussian' noise which has zero mean and constant variance. Thus, a zero-mean noise and a small positive constant variance of 0.1

are assumed. In the simulation, the antenna individual elements spaced is fixed at half-wavelength, 0.5λ. Figs. 10 and 11 show an example of how 3D beampattern steering simulation is done. The targeted CubeSat is tracked every 2.5 seconds with the optimum beam pattern. The beampatterns started to produce unwanted beams and rapidly steered towards a random target at an initial state (as soon as CubeSat reached AOS). The magnitude of the initial pattern is determined by the initial (arbitrary) choice of weights, w. This interference phenomenon causes the beams field to be canceled or doubled simultaneously where it reduces the side lobes levels besides narrowing the main lobe [11]. The main beampattern direction is then steered to track the desired CubeSat (as CubeSats move and change its elevation and azimuth. As the steering process of beampattern continued, side lobes started to appear immediately when CubeSat reached maximum elevation. The LMS algorithm calculates a new main beam pattern for the CubeSat's next position 2.5 seconds later. To calculate the new beam pattern for the new CubeSat position, it takes a maximum of 1.6 seconds for planar array and 0.7 seconds for circular array on a laptop computer equipped with CPU Intel Core i7 8th Gen which cost about 1,000 USD. As the CubeSat approaching near LOS, the side lobes power level is reduced simultaneously in the unwanted direction (side lobes reduction process). Finally, the targeted CubeSat reached LOS and the main beam pattern level is reduced and side lobes are randomly produced. The magnitude of the final pattern is determined by the strength of the interfering signal and the noise in the system.

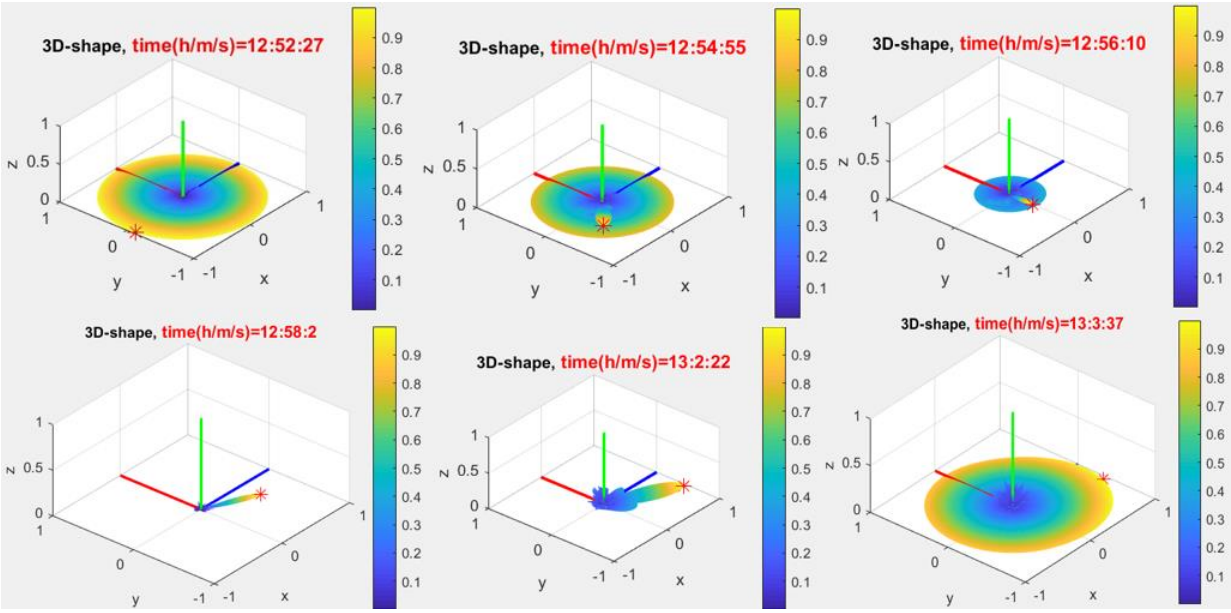

(a)

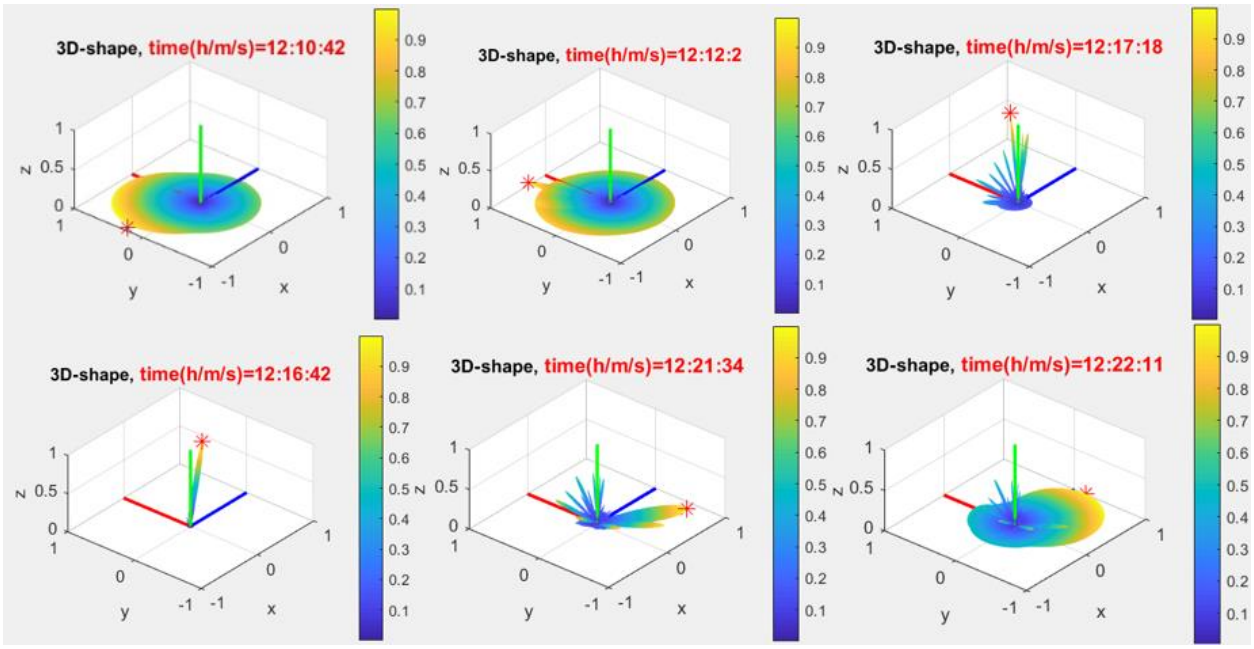

(b)

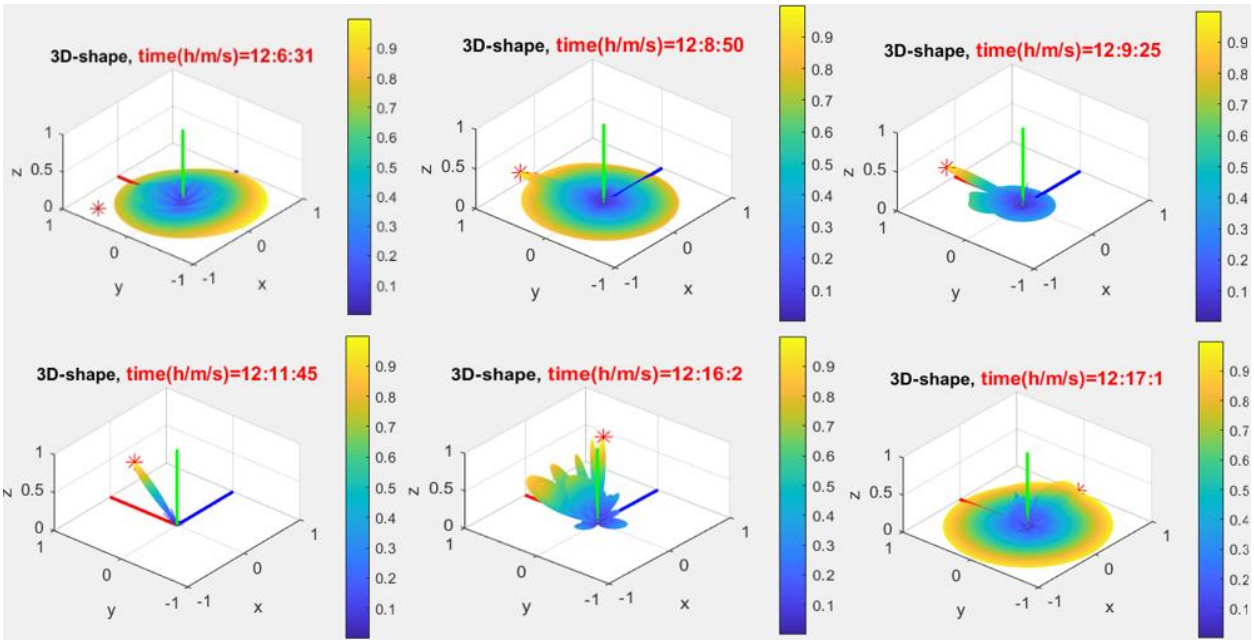

(c)

Figure 10: 3D beampattern steering plot of 27×27-elements planar array from AOS to LOS for (a) scenario 1 (b) scenario 2 and (c) scenario 3.

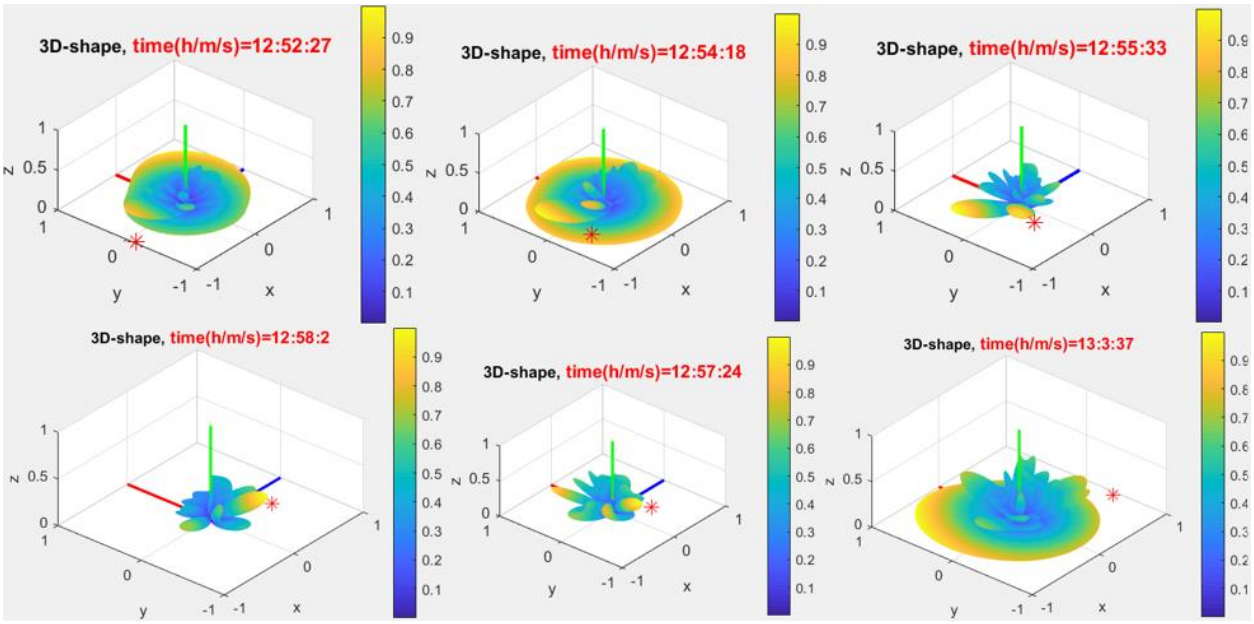
3D-shape, time(h/m/s)=12:52:27
3D-shape, time(h/m/s)=12:54:18
3D-shape, time(h/m/s)=12:55:33
3D-shape, time(h/m/s)=12:58:2
3D-shape, time(h/m/s)=12:57:24
3D-shape, time(h/m/s)=13:3:37

(a)

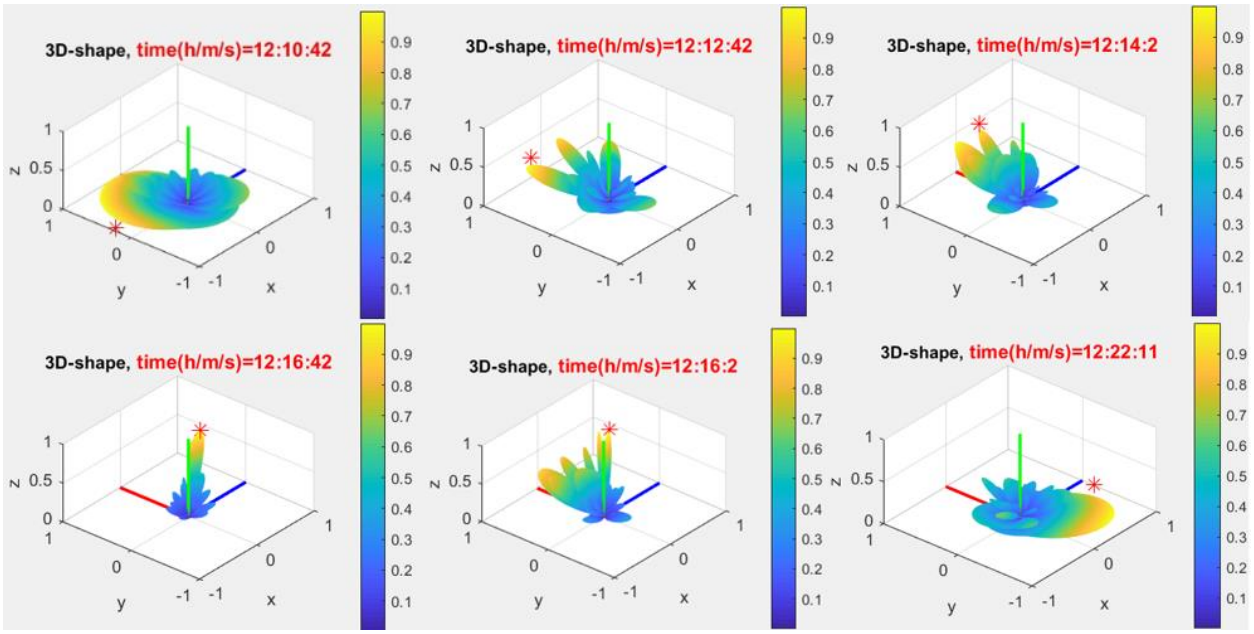
3D-shape, time(h/m/s)=12:10:42
3D-shape, time(h/m/s)=12:12:42
3D-shape, time(h/m/s)=12:14:2
3D-shape, time(h/m/s)=12:16:42
3D-shape, time(h/m/s)=12:16:2
3D-shape, time(h/m/s)=12:22:11

(b)

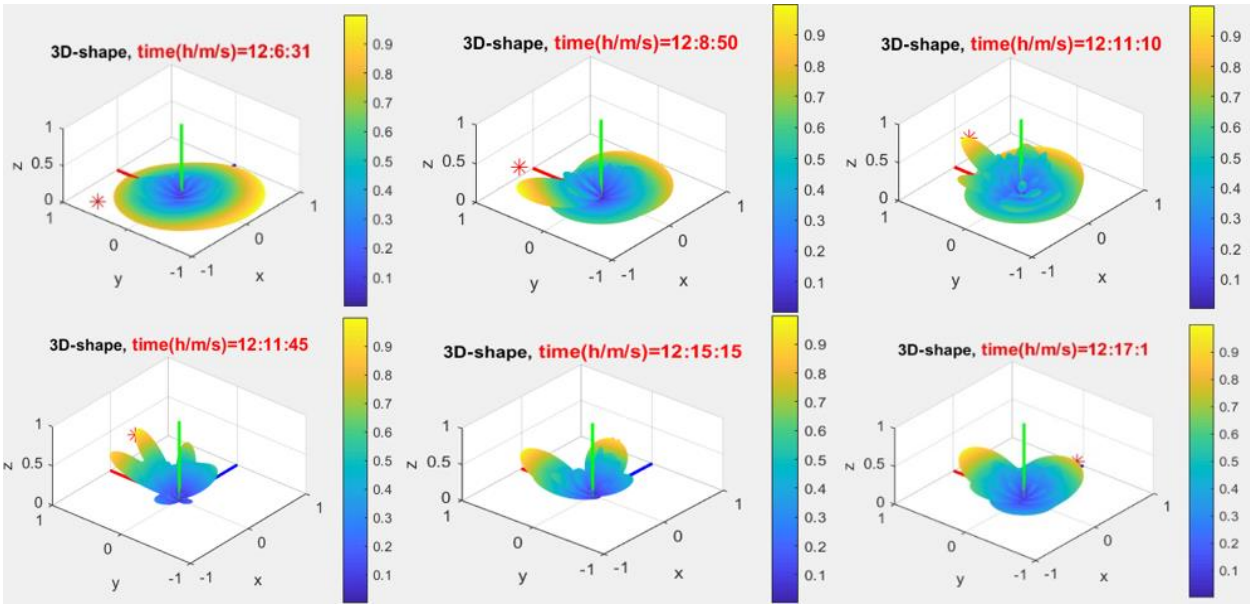

(c)

Figure 11: 3D beampattern steering plot of 729-elements circular array from AOS to LOS for (a) scenario 1 (b) scenario 2 and (c) scenario 3.

The magnitude of the AF is normalized so that the peak of the AF is unity (3D simulation result) or 0 dB (2D simulation result). A minimum AF threshold of -40 dB is set to achieve the visibility of the main lobe and side lobes. The number of data samples is set to 500 iteration samples. The weight determines the amplitude and phase which produces beampattern. The behavior of the beampattern shows the strength and direction of the desired/interfering signal in the system. In the simulation of the LMS algorithm in MATLAB software, there is one SOI at the angle of arrival from the targeted CubeSat and multiple SNOI at the side lobe part. To analyze the ability of the algorithm which gives a maximum SIR (gain) in the direction of SOI and while placing null in the direction of SNOI, simulations were performed by applying the value of different interference signal directions with the three different real-time scenarios.

By using to the input parameters in Table 2, the 2D AF rectangular beampattern plots (at azimuth and elevation angle) of SOI and SNOI are shown in Figs. 12 and 13 for Scenario 1, 2 and 3, respectively, considering 729 antenna elements for both planar and of circular arrays. The beam generates plots of AF(dB) versus azimuth and elevation angle ranging from 0º to 360º (azimuth) and 0º to 90º (elevation) in steps of 100º (azimuth) and 20º (elevation) which caused the main beam

to steer to the desired directivity corresponded with the highest AF value and narrowest beam width. The targeted CubeSat is tracked at the maximum elevation angle (considering that 729 planar array antenna elements track the CubeSat) to avoid the 'end-fire steering' directivity phenomenon where the beam is steered parallel to Earth ground level. The possibility of not able to track the desired CubeSat is higher when the CubeSat elevation angle is less than 10º.

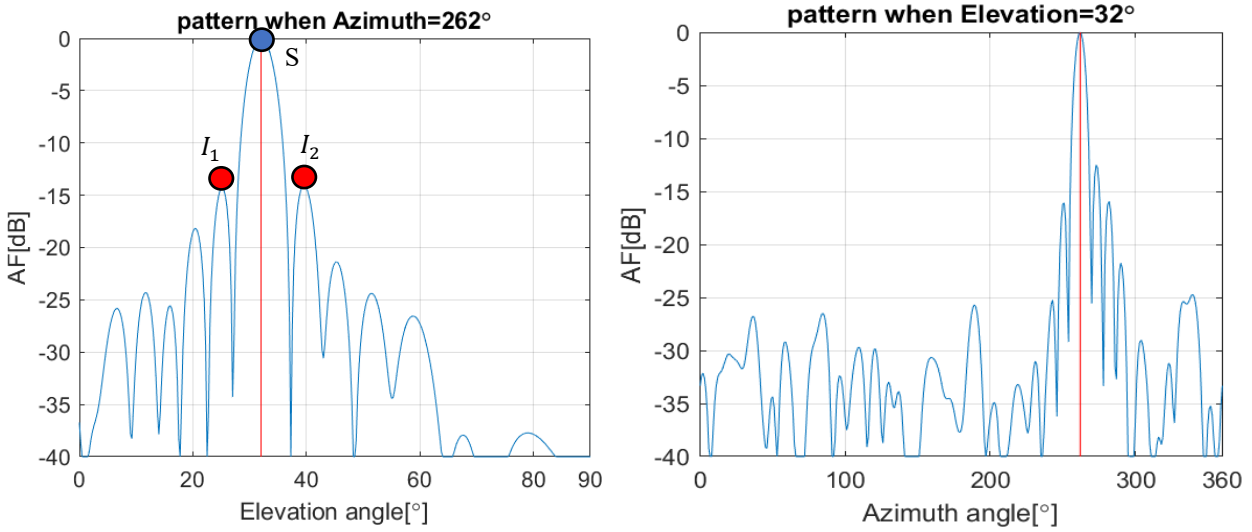

(a)

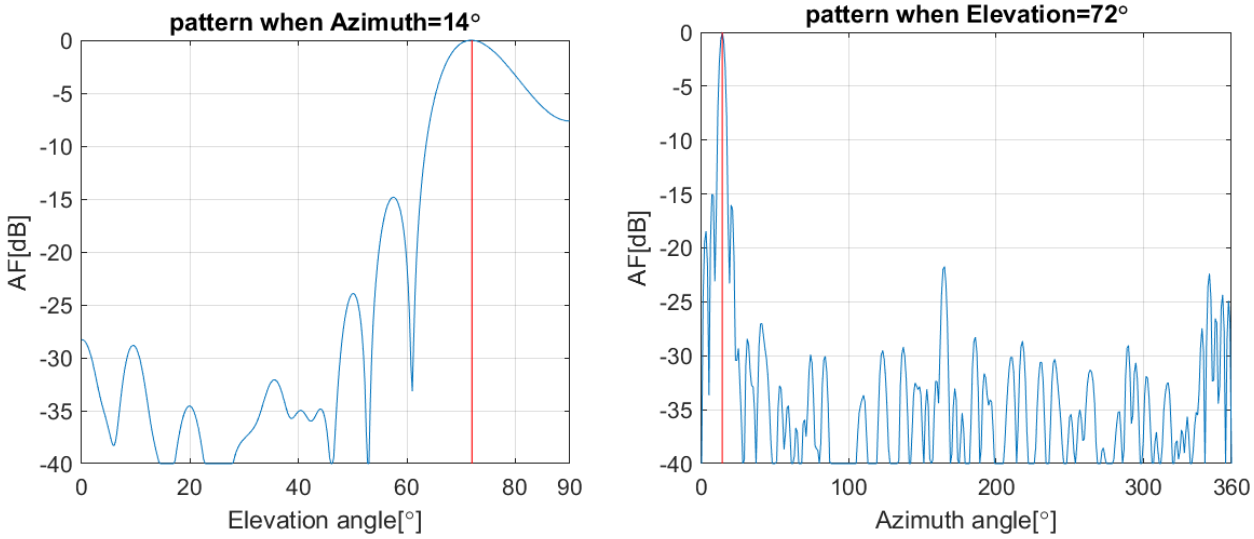

(b)

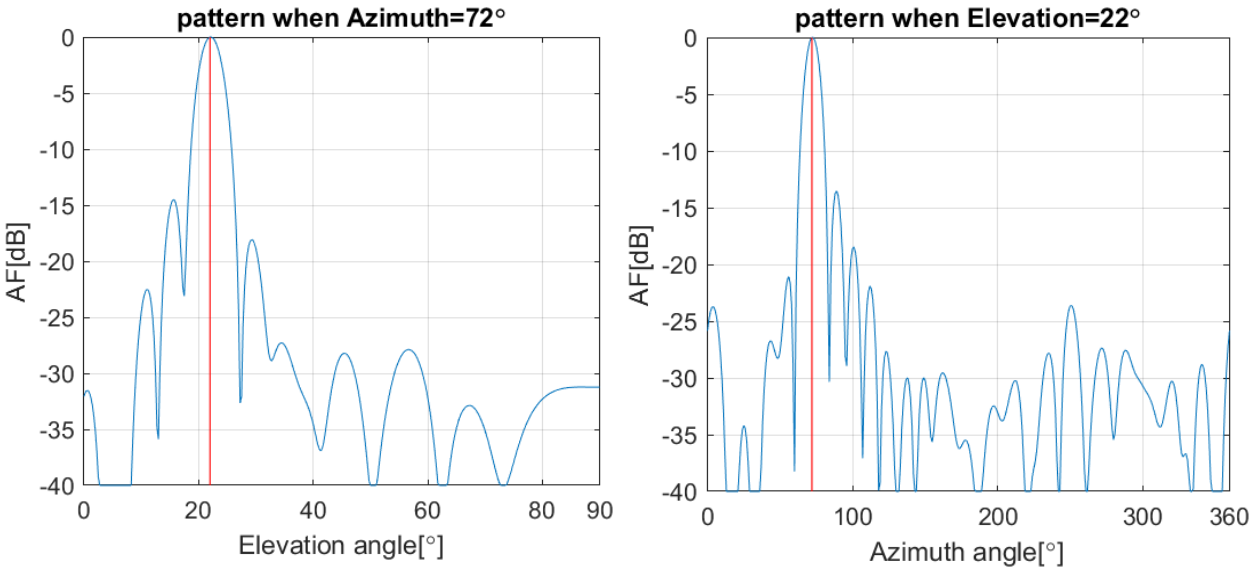

(c)

Figure 12: 2D normalized AF of 27×27-elements planar array for (a) scenario 1 (b) scenario 2 and (c) scenario 3.

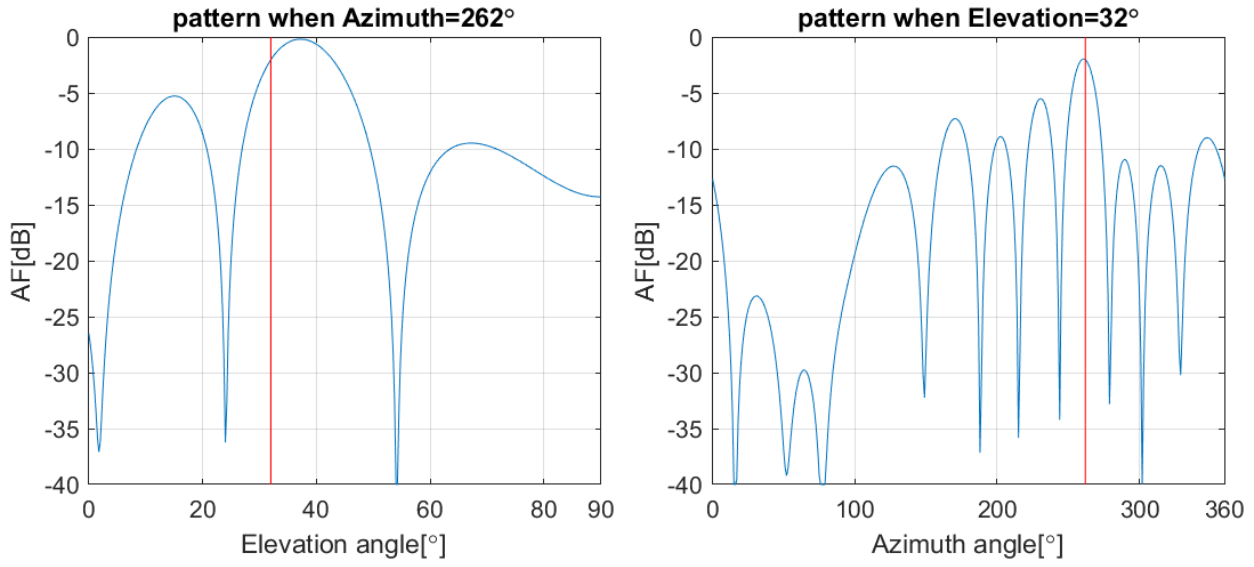

(a)

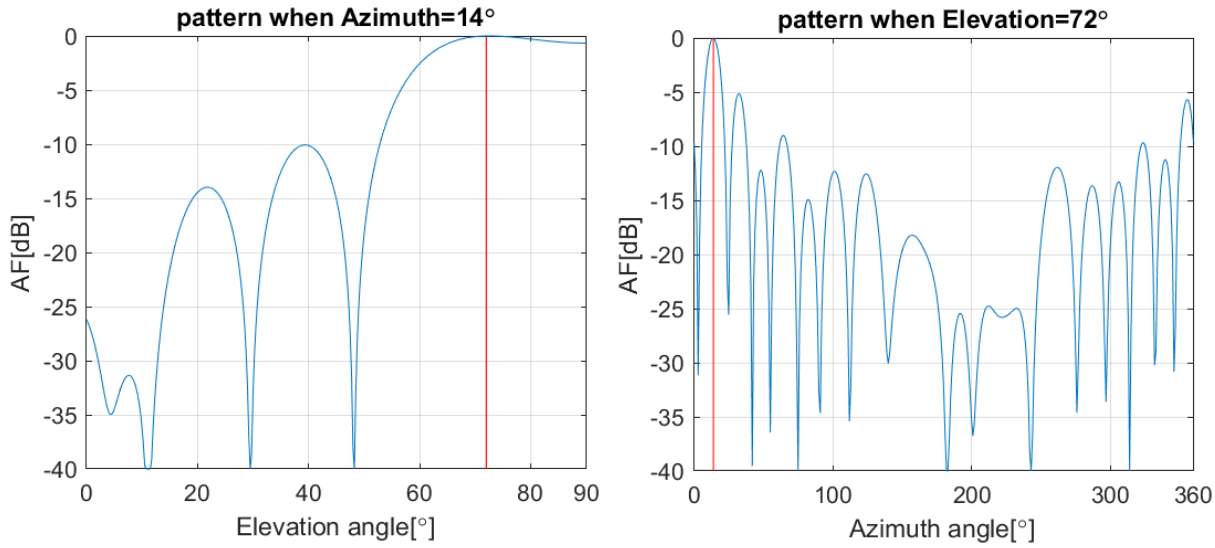

(b)

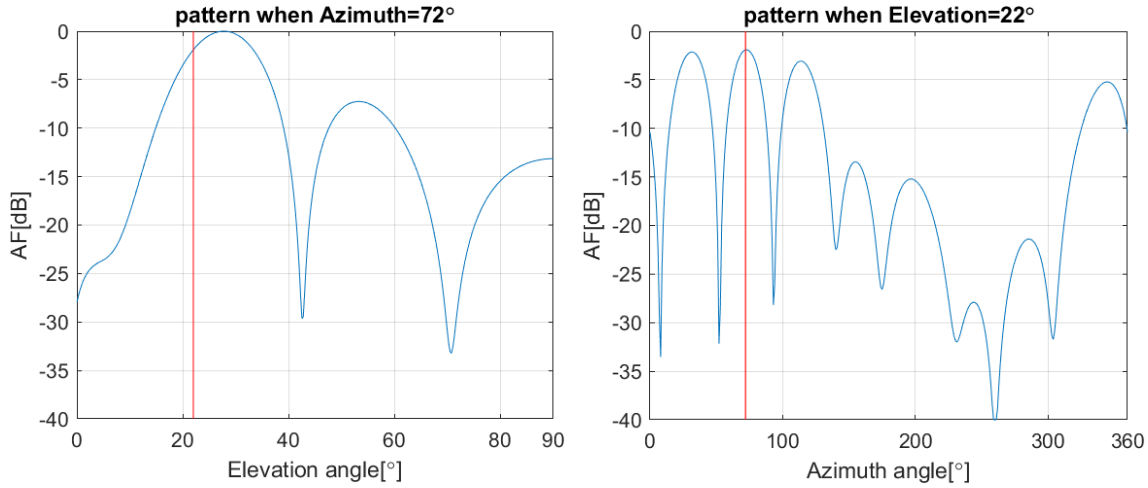

(c)

Figure 13: 2D normalized AF of 729-elements circular array for (a) scenario 1 (b) scenario 2 and (c) scenario 3.

Details information represented by Figs. 10 and 11 (2D AF intensity distribution which beampattern at maximum elevation, viewed from top, azimuth and elevation angle) for planar and circular array is shown in Figs. 14 and 15. The red asterisk marked on the main beam peak indicates the position of targeted/tracked CubeSat. The implementation of the LMS algorithm shows the

ability to track the desired CubeSat passes (within AOS and LOS) for three different scenarios while minimizing side lobes of other interference CubeSats, simultaneously.

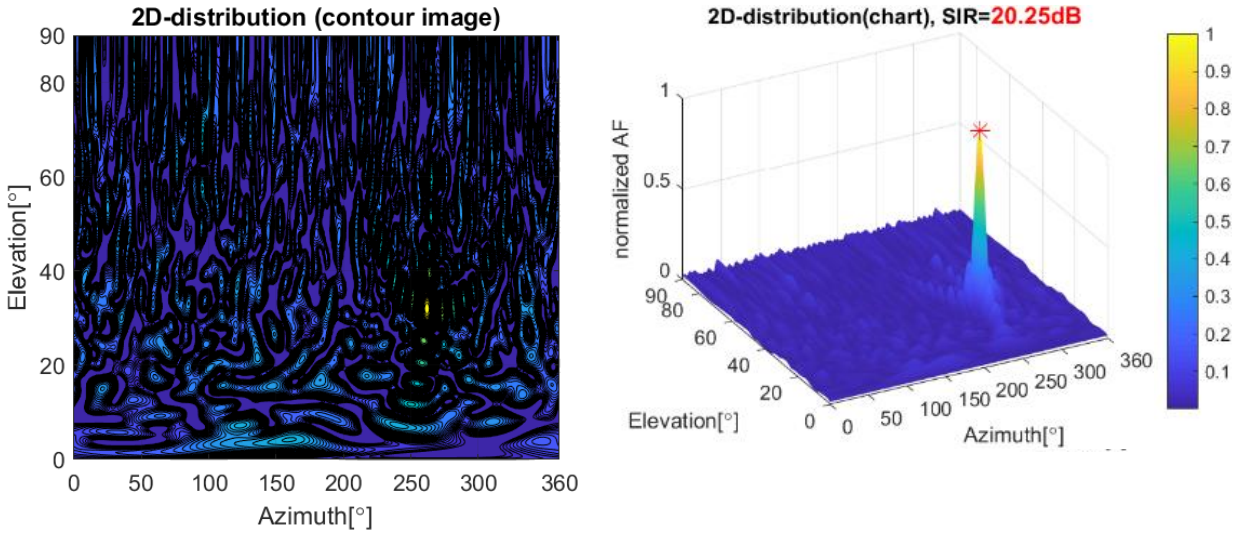

(a)

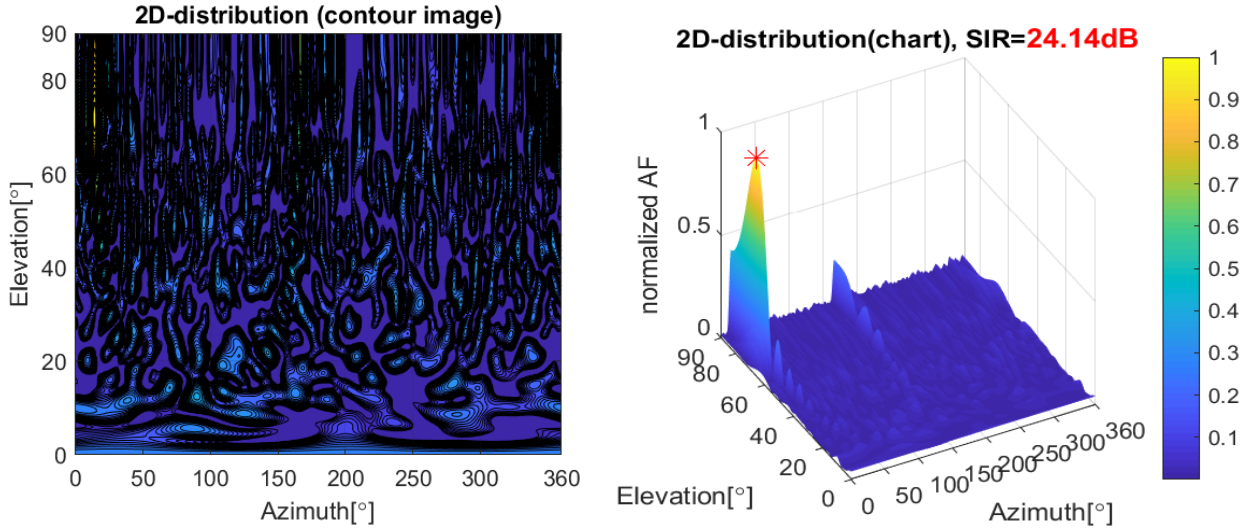

(b)

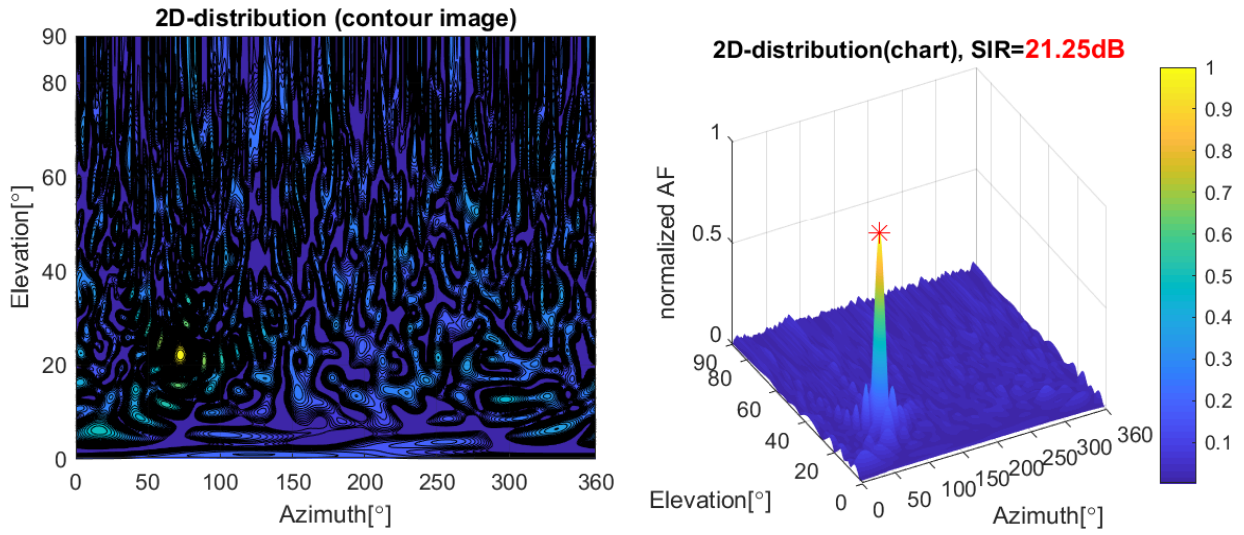

(c)

Figure 14: 2D AF intensity distribution of 27×27-elements planar array for (a) scenario 1 (b) scenario 2 and (c) scenario 3.

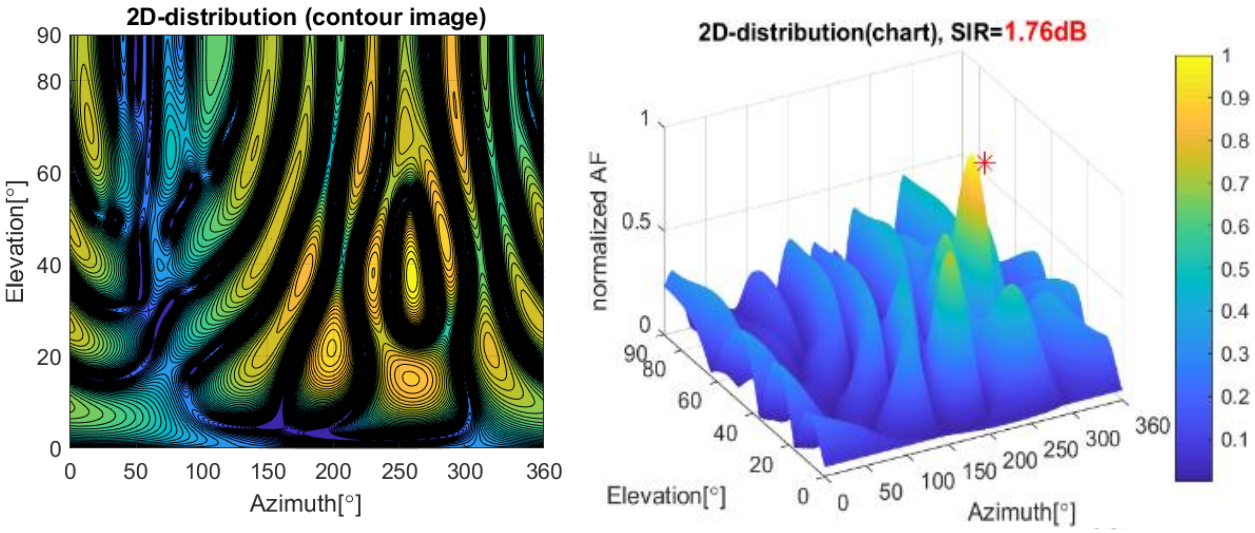

(a)

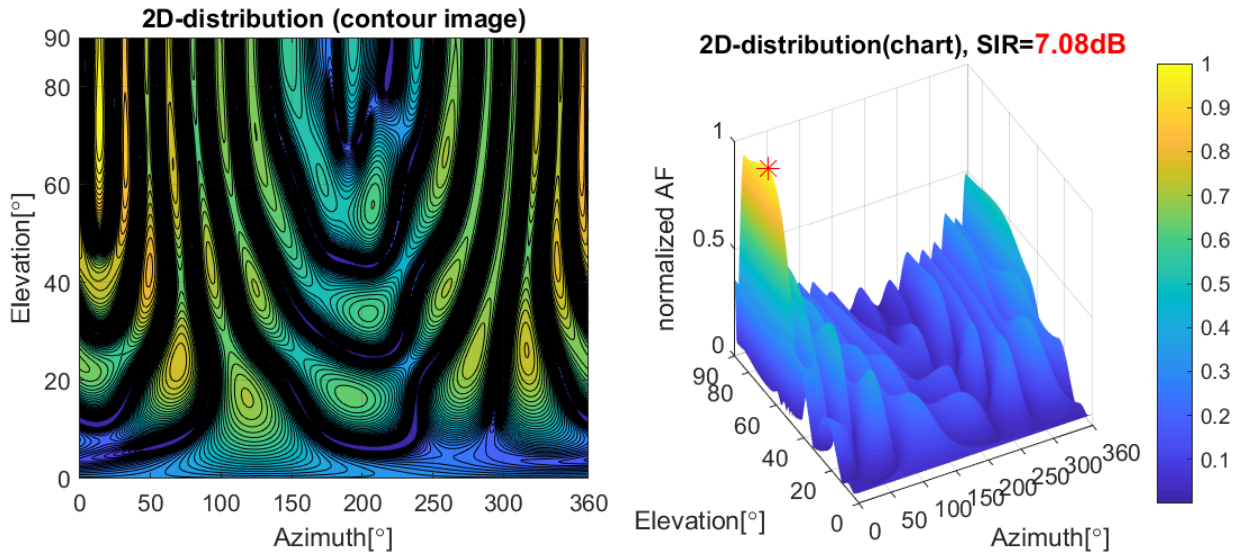

(b)

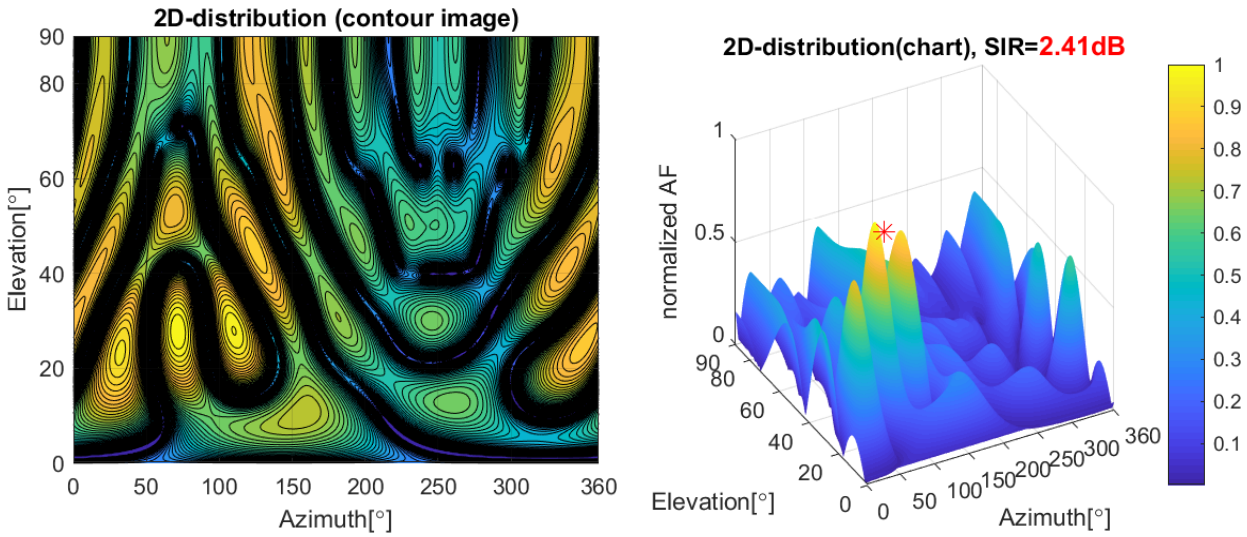

(c)

Figure 15: 2D AF intensity distribution of 729-elements circular array for (a) scenario 1 (b) scenario 2 and (c) scenario 3.

Signal-to-Interference Ratio (SIR) is defined as the ratio of the desired signal power to the undesired signal power. The red lines in Figs. 12 and 13 indicate the elevation and azimuth angle mark for the 2D azimuth plot describing the targeted CubeSat. The SIR values are derived by using Eqs. (18) and (19) as follows:

$$SIR(mW) = S(mW)/I_1(mW) + I_2(mW) \quad (18)$$

$$SIR(dB) = 10\log\left(SIR(mW)\right) \quad (19)$$

The 2D AF rectangular plots of radiation pattern for Scenario 1 of planar array in Fig. 12(a) shows the value SIR of the main beam to the first side lobe about 20.25 dB at the elevation angle of 32°. In Scenario 2 and 3 for planar array, the SIR are 24.14 dB (el = 72°) and 21.25 dB (el = 22°). Results show that Scenario 2 produces the highest SIR compared to the SIR results from Scenario 1 and 3. Fig. 13 shows the SIR results for circular array. As for Scenario 1, 2 and 3 in Figs. 13(a), 13(b) and 13(c), the calculated SIR is 1.76 dB (el = 32°), 7.08 dB (el =72°) and 2.41 dB (el = 22°), respectively. The results of SIR for all scenarios are summarized in Table 4.

Table 4: Signal-to-Interference Ratio of Each Scenario. The Value at the Maximum Elevation of the Targeted CubeSat is Shown.

Scenario	Array type	Elevation (º)	SIR (dB)
1	Planar	32	20.25
2	Planar	72	24.14
3	Planar	22	21.25
1	Circular	32	1.76
2	Circular	72	7.08
3	Circular	22	2.41

The SIR value changes as the antenna track the target CubeSat and form the beam pattern. In Fig. 16, the temporal variation of the SIR value from AOS to LOS is plotted for Scenario 1 and 3. The CubeSat tracked by 27×27 elements planar array antenna.

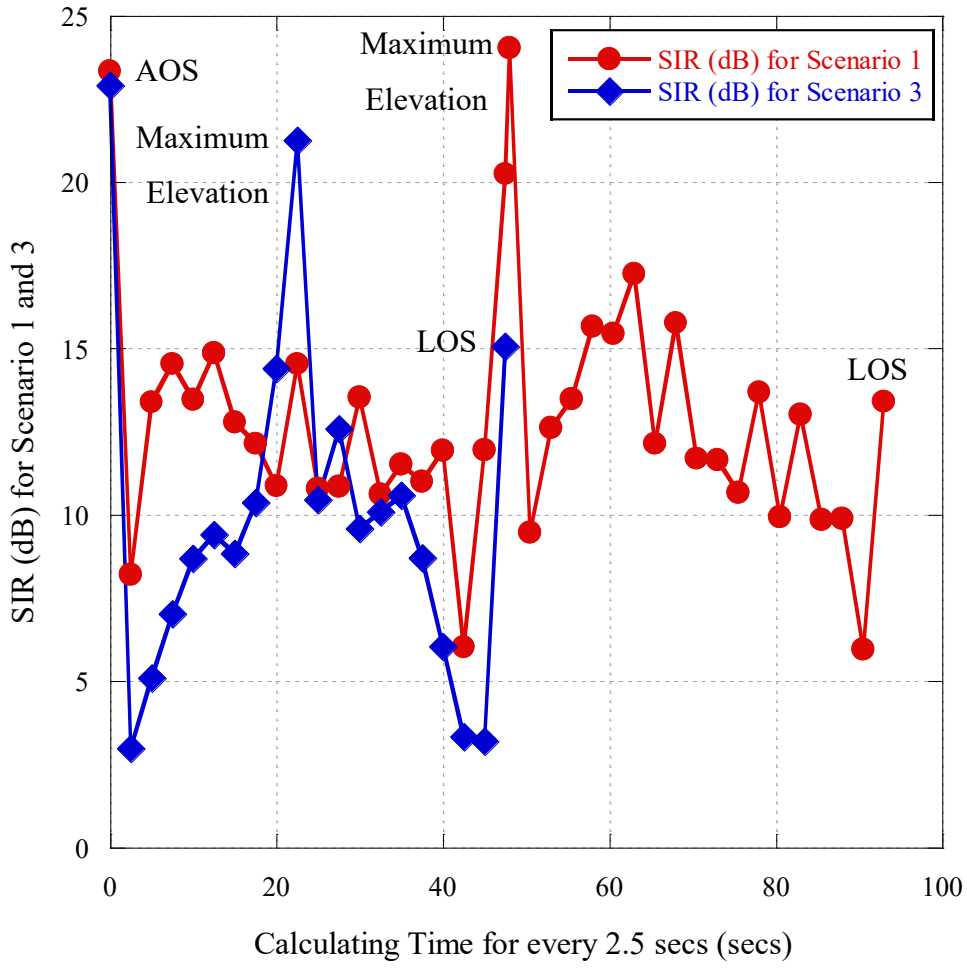

Figure 16: Temporal variation of SIR for scenario 1 and 3 for every 2.5 seconds CubeSat tracked by 27x27 elements planar array from AOS to LOS.

The SIR value experiences a sudden high peak for both Scenario 1 and 3 as soon as CubeSat tracking is started during AOS. The SIR for Scenario 1 decreases instantaneously, 6.03 dB at 42.5 seconds before the targeted CubeSat reaching the maximum elevation. In contrast to Scenario 3, the SIR experiences only a slight decrement of 8.84 dB at 15 seconds before the targeted CubeSat reaching the maximum elevation. Furthermore, the significant increment of SIR for both scenarios can be noticed as the targeted CubeSat is at the maximum elevation. This phenomenon happens when the adaptive planar array antenna tries to adjust the weights and steer the null of the array in the direction of the interferer CubeSats. As the iterative process progresses, the magnitude pattern will change to null-out the interfering signal (from the interferer CubeSat direction) and focus on

the SOI (from the targeted CubeSat). A trend of the lowest SIR significant decrement of 5.95 dB at 90.5 seconds (Scenario 1) and 3.19 dB at 45 seconds (Scenario 3) just before the targeted CubeSat approaching LOS. The decrement trends in SIR (for both scenarios) which happened just after the targeted CubeSat leaving AOS is because the beam patterns started to produce unwanted beams and rapidly steered towards a random target at an initial state. On the other hand, the significant decrement when the targeted CubeSat approaching LOS is caused by the reduction of the main beam pattern level and randomly produced side lobes.

In LEO satellite communications where the elevation angle of transmission path changes continuously, the distribution of elevation angles must be considered for obtaining the overall SIR statistics. SIR result shown in Fig. 16 is the temporal variation of SIR calculation for every 2.5 seconds from AOS to maximum elevation angle to LOS, for both Scenarios 1 and 3. The highest SIR values for both Scenario 1 and 3 are when the CubeSats are at the maximum elevation angle, proving that the SIR keeps increasing as the elevation angle keeps increasing. The gradual SIR increment indicates that the signal strength is reaching the maximum value when the CubeSat is at the maximum elevation. Consequently, the investigation on the effects of the number of antenna elements and the array type, planar and circular in terms of SIR and CPU time are considering CubeSat is at the maximum elevation angle.

Figs. 17 and 18 show the result of SIR and CPU time as the number of antenna elements is increased for both planar and circular array, considering all scenarios. Based on the SIR results in Fig. 17, it shows that the planar array configuration for all scenarios produces a significantly higher SIR result compared to the circular array configuration for all scenarios. This is due to the existence of a higher side lobes level in the circular array beam pattern compared to the planar array beam pattern. The presence of side lobes that approaching the level of the main lobe will minimize the SIR, making the array antenna vulnerable to noise and interference signals. The planar array arrangement increases the array steering capability as well as reducing the sidelobe levels.

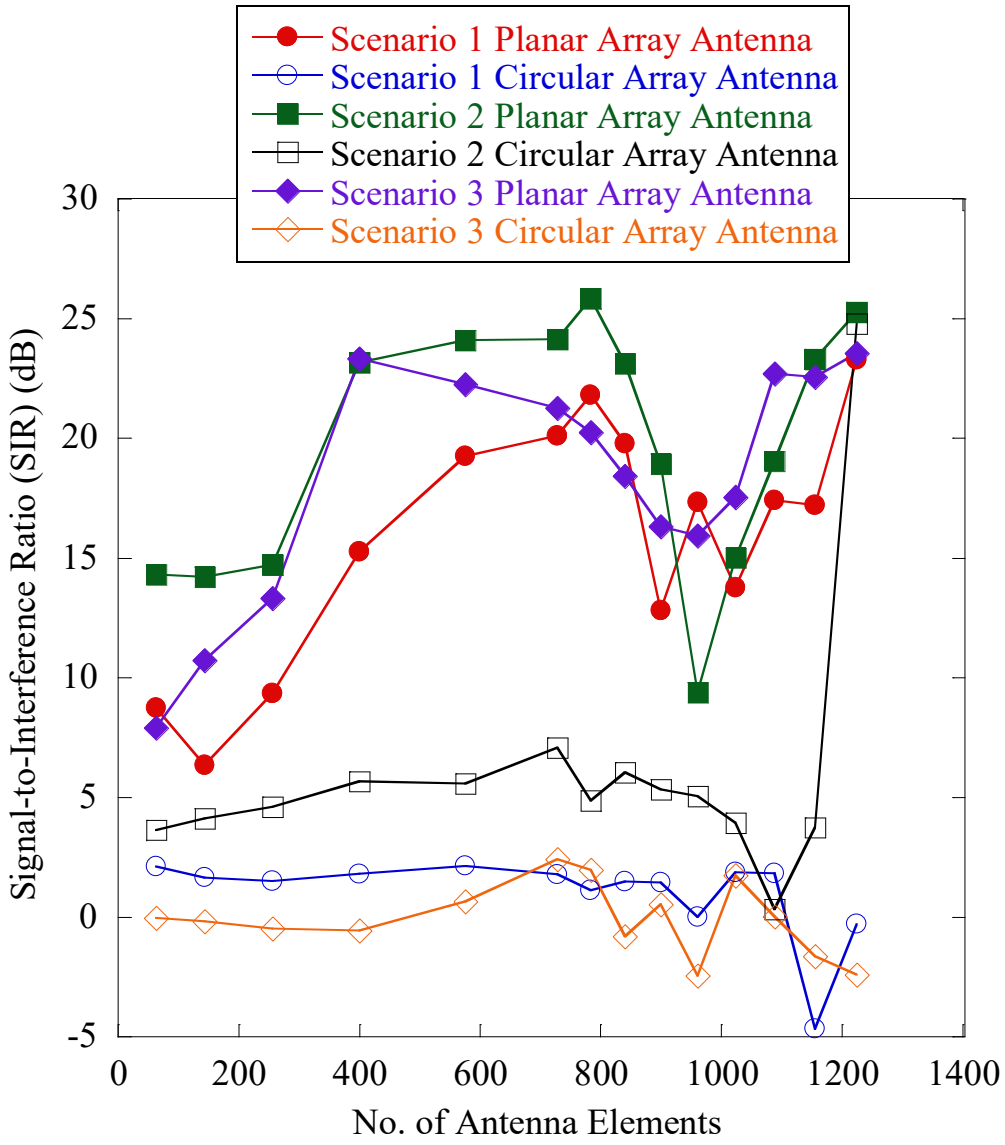

Figure 17: SIR of planar and circular array antenna at the maximum elevation for three scenarios of CubeSats constellations.

CPU time is an empirical result that relates to the computational complexity of the algorithm used. The purpose of calculating the CPU time is to evaluate the performance of the beamformer implemented using the LMS algorithm in an environment with multiple interference signals. Fig. 18 illustrates the CPU time taken to produce the new beam pattern at every 2.5 seconds during the simulation.

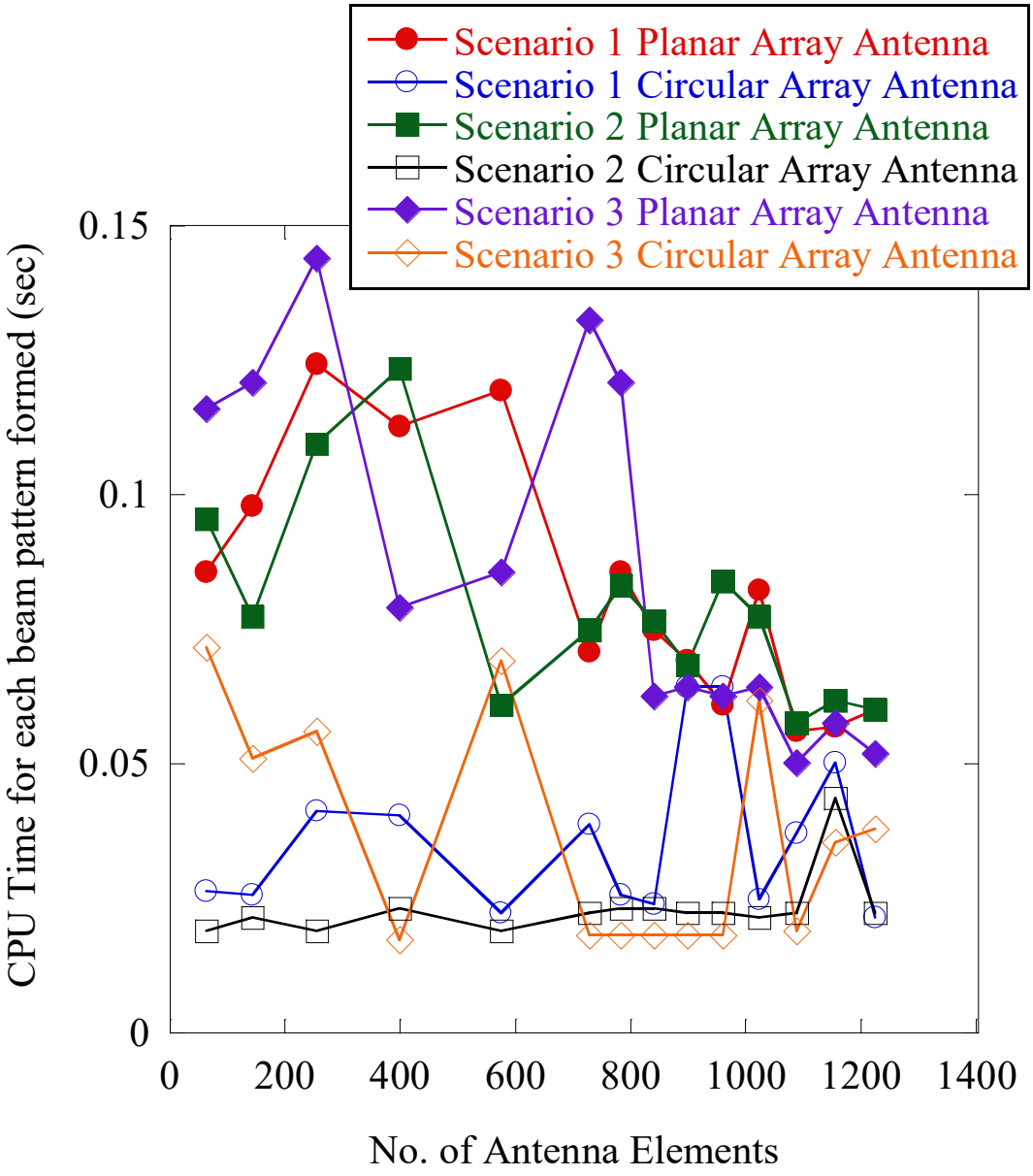

Figure 18: CPU time of planar and circular for three scenarios of CubeSats constellations.

The CPU time longer than 2.5 seconds means that the computer is not capable of making the new beam pattern on time. A higher performance computer is needed, or the antenna configuration needs to be changed. The result verifies that the LMS algorithm simulated for the circular array antenna is averagely much faster than for the planar array antenna for all scenarios. The circular array geometry does not have edge elements. Its ability of scanning in either azimuth or elevation directions and have uniform resolution over the azimuth but nonuniform resolution

over the elevation. Without edge constraints, the beam pattern of a circular array can be electronically rotated and scanned in an azimuthal plane without significant change in beam shape. Because of these advantages, the computational complexity of the LMS algorithm simulated for the circular array antenna based on the CPU time is much lesser than the planar array antenna. On the other hand, the higher number of side lobes (interference signals) present in the circular array antenna is less likely to impact the computational of the algorithm.

Based on their performance and the concept of AAA replacing the traditional big dish antenna for GS is proved. Starting with a uniform 8×8 elements for planar antenna array and 64 elements with 2 meters radius for circular antenna array, the number of antenna elements is increased until a total of 1225 and the beampattern performance is analyzed. By setting a constant radius of 2 meters for the circular array antenna configuration, there is no significant effect in SIR result and the effect of mutual coupling between the elements, as the number of antenna elements are increased. This is due to the capability of the circular array antenna to compensate the effect of mutual coupling by breaking down the array excitation into a series of symmetrical components.

It is interesting to see beyond 800 elements, there is no improvement in the SIR until reaching the 1000 elements. Also, it is interesting to see that CPU time does not depend on the number of antenna elements. This is because of the CPU time relates to the computational complexity of the algorithm to calculate two different array antenna geometry (related to the Degree of Freedom). Degree of Freedom happens to multiple antenna system, which size, area, geometry & physical constraints. The array size determines how many basic functions are significant or easy to excite. In other words, the array size determines the resolvability over the propagation space. Given the size of arrays, these numbers form the upper bound on the number of spatial degrees of freedom independent of the number of antennas. Packing more antennas beyond these limits will not increase the channel capacity significantly. The CPU time for the planar array is inversely proportional to the number of array antenna elements. This is due to the increment number of the planar array arrangement which also increases the main beam steering capability in both elevation and azimuth angles and finally reduces the side lobes fast.

In the real implementation of the AAA, the exact position of each CubeSat can be identified as they emit some satellite's ID (a header) which can be predicted in advance by SATPC32 software. As the CubeSats reach the GS footprint, training sequence/pilot signal (BPSK signal in this case) is sent by the GS to identify the CubeSat signal. The pilot signal is sent in proper timing

to ensure the CubeSat acknowledges that the GS is ready for tracking, transmit and receive data. After finding the targeted CubeSat, the main beampattern is optimized, improving the SIR and produces optimum beampattern.

Training sequence or pilot signal is a known reference or desired signal, $d(t)$ that transmitted a series of bits, periodically by the transmitter which are known in advance at the receiver. Figs. 14 and 15 demonstrate that as the training sequence or pilot signal (BPSK signal) is corrupted by the noise in the environment (interference from nearby CubeSats), the adaptive arrays will then adjust the weights and steer the null of the array in the direction of the interferer CubeSats. As the iterative process progresses, the magnitude pattern will change to null-out the interfering signal (from the interferer CubeSat direction) and focus on the SOI (from the targeted CubeSat). The convergence of the algorithm depends on the input parameter, step-size value, μ which controls the rate of adaptation.

In the principle of beamforming, a signal processing technique is implemented into combining array antennas in such a way that signal in a particular angle experience constructive interference (maximize the desired beam) while other signals will experience destructive interference (minimize the unwanted beam). From the 3D simulation plots, the LMS algorithm shows the ability to suppress side lobes (interference signals from interferer CubeSats) by putting nulls and steer the main beam towards the desired signal (targeted CubeSat). Planar array antenna (for all scenarios) produces the narrowest main 3-dB beamwidth compared to the circular array antenna. The output of SIR is maximized and the MSE is minimized as much as possible.

Mean Square Error (MSE) is similar to Signal-to-Noise Ratio (SNR) except that it accounts for interference in addition to noise power. The acceptable MSE values of each transmitting (T_x) and receiving (R_x) are evaluated to verify the link is operating as expected. Figs. 19 and 20 show the MSE plots of planar and circular array antenna tracked by 27x27 elements at the maximum elevation angle for Scenario 1, 2, and 3, respectively. Based on the results of the MSE plot in Fig. 19, MSE has hesitation at the beginning of the iterations with an approximate maximum value of 1.0 for all scenarios. After 10^{th} iterations, the convergence occurs and the MSE level reaches zero. However, circular array antenna shows different MSE plots wherein Scenario 1, the MSE is ranging from 0.02 to 0.22 at iterations, i from 5^{th} to 48^{th}, after 48^{th} iterations, the convergence occurs and the MSE level decrease approaching zero, even though experience some fluctuations. However, in Scenario 2, the MSE has hesitation at the beginning of the iterations with a maximum

value of 1.0 and after 80th iterations, the convergence starting to occur, and finally the MSE level reaches zero value. Scenario 2 MSE plot shows a fast convergence because of the inter-satellite interference is not significant for the constellation in Scenario 2 as the nearby interferer satellites within the same footprint are only three satellites. In Scenario 3 MSE plot, the MSE started to reduce from 1.0 to 0.35 at iterations, i from 0th to 5th. After the 5th iterations, the convergence occurs and the MSE level still experience fluctuations as it tries to reach zero MSE value. From the MSE results Figs. 19 and 20, it proved that the LMS algorithm is fairly robust to the changing environments.

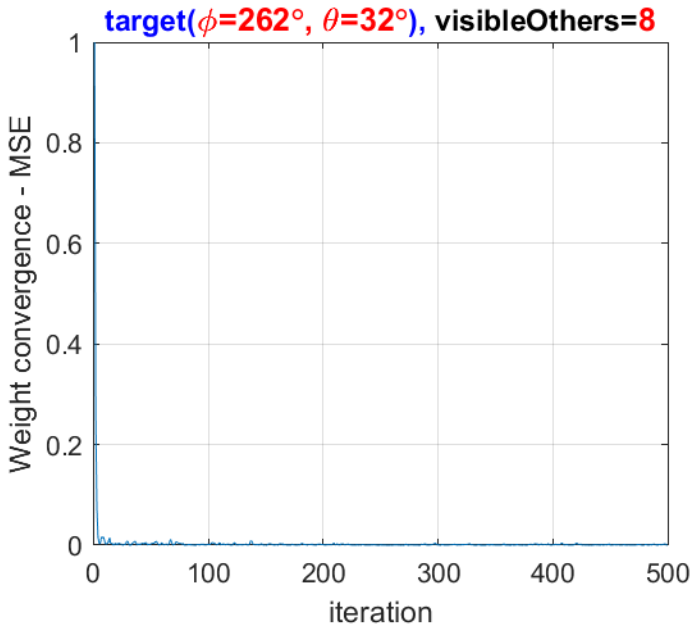

(a)

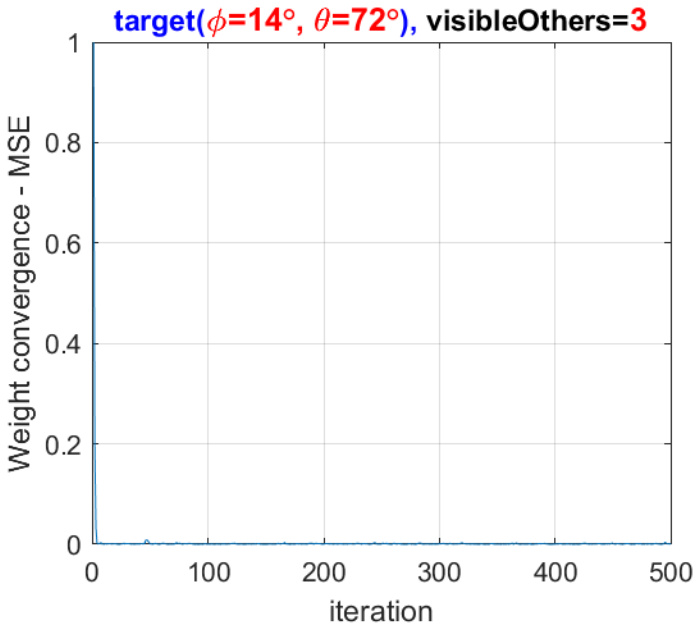

(b)

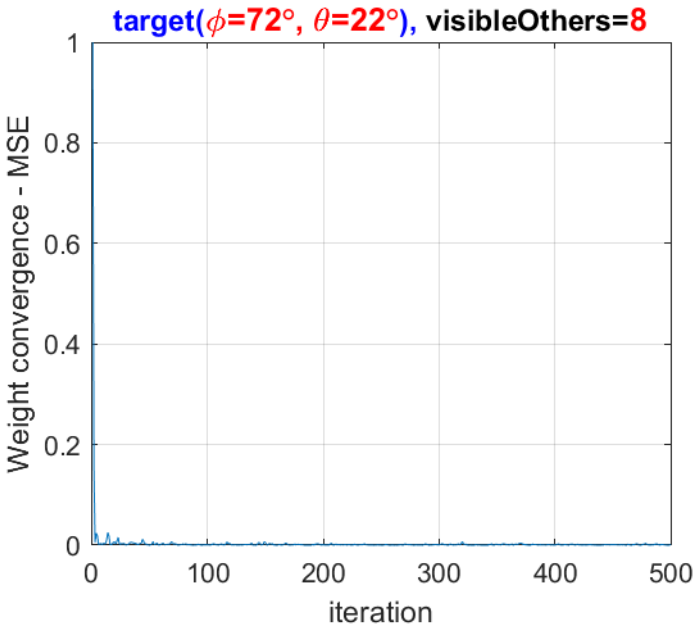

(c)

Figure 19: MSE plots of planar array antenna tracked by 27x27 elements at the maximum elevation angle for (a) Scenario 1, (b) Scenario 2 and (c) Scenario 3

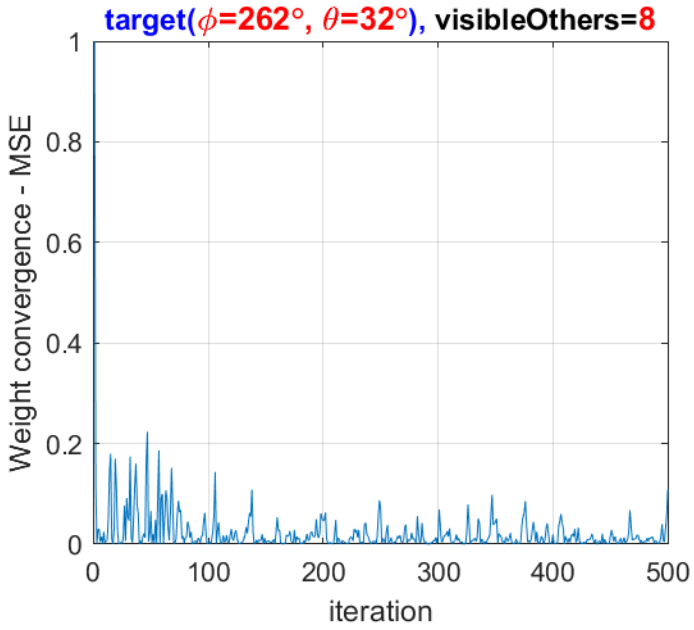
target(ϕ=262°, θ=32°), visibleOthers=8
Weight convergence - MSE
iteration
0
0.2
0.4
0.6
0.8
1
0
100
200
300
400
500

(a)

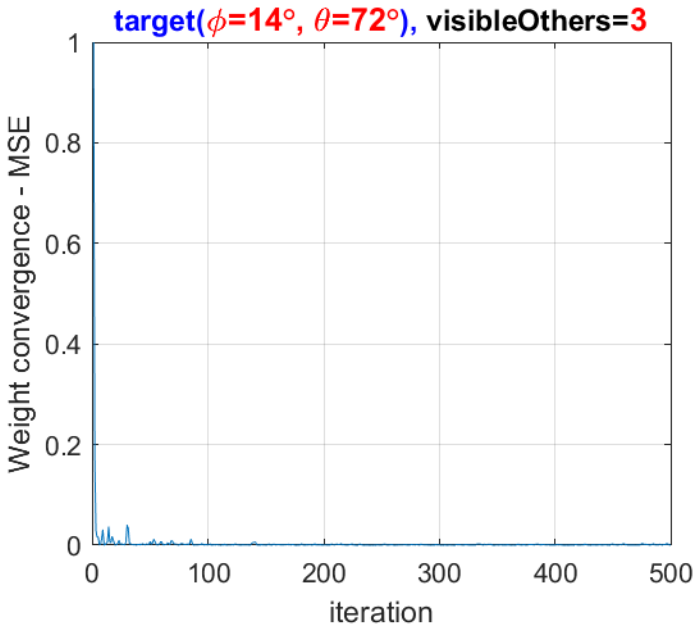
target(ϕ=14°, θ=72°), visibleOthers=3
Weight convergence - MSE
iteration
0
0.2
0.4
0.6
0.8
1
0
100
200
300
400
500

(b)

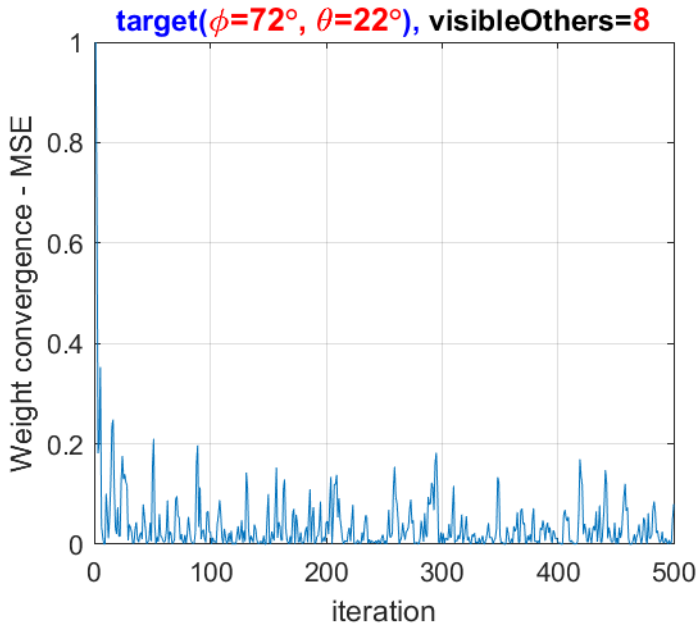

(c)

Figure 20: MSE plots of circular array antenna tracked by 27x27 elements at the maximum elevation angle for (a) Scenario 1, (b) Scenario 2 and (c) Scenario 3

CHAPTER 5

CONCLUSION AND RECOMMENDATION

5.1 Conclusion

It was concluded that the implementation of LMS algorithm in AAA is more reliable and suggested to be adapted in GS tracking control system, replacing the big dish traditional GS antenna system with the manually controlled system. Results and analysis show the maximum beam pattern received at the appropriate angle towards the targeted CubeSat. Its ability to perform electronically steerable beam scanning, precise targeting and fast-tracking even for tracking a massive LEO CubeSats constellation, proved that the implementation of AAA for a GS system is the most promising solution [10]. Moreover, its capability to mitigate the effect of interference from the nearby CubeSats, improves the link quality and therefore provides better coverage and increase capacity. As most of the small constellation satellites builders and researchers recently did a lot of research work on the AAA, there are still some technical challenges due to the high cost and massive scale of building the whole architecture within a short period.

5.2 Contribution

Soon, more small satellites including CubeSats will be deployed in a massive constellation batch by batch utilizing the LEO. A reliable GS antenna system such as AAA is a promising advanced technology which provides continuous coverage for LEO CubeSats and this will change the future mission paradigm, indirectly. AAA technology at the GS is believed will provide basic building blocks for future flexible cost-effective wireless network for satellites and continuous coverage. As the diversity of the small satellites keep increasing day by day, the complexity of signal transmissions from satellites will also increase and thus the interference will be increase, continuously. Due to this advance of space technology, there is needs for more sophisticated management of signal spectrum that can be provided by the AAA GS.

5.3 Recommendation for Future Work

One of the emerging technologies of GS antenna used these days is phased array antenna with electronically steerable beam scanning (flat panel antennas), which also known as adaptive

array antenna (AAA). The steering of AAA is high in speed or perhaps instantaneous and the field of view during steering may cover a wide range which is within the range of +/- 60 degrees [1]. Due to these advantages, adequate steering can be executed even for a massive CubeSats constellation. Signal interference can be reduced with the implementation of the proposed GS system as it can perform precise tracking in a free space condition. The array antenna pattern is reshaped to narrower beam width, adapting with the signal environment while tracking to the exact elevation and azimuth angle of the targeted CubeSat and hence, the signal quality is enhanced, and link quality is improved. The degradation performance at the GS side is possible to be mitigated.

With advances in microwave monolithic integrated circuit (MMIC) and packaging technologies, the AAA has been evolved as a strong candidate for many present and future applications in satellite communications.

REFERENCES

[1] K. Dredge, M. V. Arx and I. Timmins, LEO Constellations and Tracking Challenges, *Satellite Evolution Group Article, (2017),* 36-38.

[2] C. Yao et al, Satellite Ground Stations with Electronic Beam Steering in IEEE, *2012 IEEE First AESS European Conference on Satellite Telecommunications (ESTEL), (2012), 1-7.*

[3] M. Hu, W. Tang, and C. Cai, A new Variable Step-Size LMS Adaptive Filtering Algorithm for Beamforming Technology in IEEE, *9th International Symposium on Antennas, Propagation and EM Theory (ISAPE), (2010),* 101-104.

[4] W. A. Ali, D. A. Mohamed, and A. H. Hassan, Performance Analysis of Least Mean Square Sample Matrix Inversion Algorithm for Smart Antenna System in IEEE, *Loughborough Antennas and Propagation Conference (LAPC), (2013),* 624-629.

[5] S. Das, Smart Antenna Design for Wireless Communication using Adaptive Beam-Forming Approach in IEEE, *TENCON 2008-2008 IEEE Region 10 Conference (2008), 1-5.*

[6] S. Kamboj and R. Dahiya, Adaptive Antenna Array for Satellite Communication Systems, *International Multi Conference of Engineers and Computer Scientists (IMECS) 2 (2008), 1-4*.

[7] K. J. Lian, *Adaptive antenna arrays for satellite personal communication systems*, Master of Science dissertation, Dept. Elect. Eng., Virginia Polytechnic Institute and State University, Blacksburg, 1997.

[8] D. F. Breslin, *Adaptive antenna arrays applied to position location*, Master of Science dissertation, Dept. Elect. Eng., Virginia Polytechnic Institute and State University, Blacksburg, 1997.

[9] C.A. Balanis, *Antenna Theory: Analysis and Design,* fourth ed. (John Wiley and Sons, Inc., Canada, 2016, pp. 931–980).

[10] N. C. Kyun et al, Modelling and Simulation of Phased Array Antenna for LEO Satellite Tracking in Springer, Berlin, Heidelberg, *International Conference on Information Networking (ICOIN), (2002),* 359-371.

[11] S. Alio and L. Kudsi, Adaptive Array Antennas for Mobile Earth Stations: A Review, *Information Science Letters An International Journal, Inf. Sci. Lett., (2017), 6*(1), 29-32.

[12] N. Kaya and J. Mankins, New Receiving Ground Antenna using Active Phased Array Antenna for Satellites, *International Astronautical Congress (IAC), Guadalajara, Mexico, (2016).*

[13] https://www.space-track.org/#tle (accessed in May 14, 2019).

[14] Al-Sadoon, Mohammed, Raed A. Abd-Alhameed, I. Elfergani, J. Noras, Jonathan Rodriguez, and S. Jones. "Weight optimization for adaptive antenna arrays using LMS and SMI algorithms." *WSEAS Transactions on Communications* 15 (2016): 206-214.

APPENDIX A

REPORT ACCESS OF SCENARIO 1 IN STK

Facility-KyutechGS-To-Satellite-FLOCK_4A-12_44108

KyutechGS-To-FLOCK_4A-12_44108 - AER reported in the object's default AER frame

	Time (UTCG)	Azimuth (deg)	Elevation (deg)	Range (km)
	14 May 2019 11:19:53.356	124.616	-0.124	2602.199533
	14 May 2019 11:20:53.000	117.913	3.082	2268.662343
	14 May 2019 11:21:53.000	108.907	6.431	1971.869988
	14 May 2019 11:22:53.000	96.906	9.606	1735.775496
	14 May 2019 11:23:53.000	81.680	11.913	1589.132318
	14 May 2019 11:24:53.000	64.481	12.443	1558.309800
	14 May 2019 11:25:53.000	48.002	10.927	1650.107466
	14 May 2019 11:26:53.000	34.375	8.069	1846.097265
	14 May 2019 11:27:53.000	23.996	4.744	2116.916262
	14 May 2019 11:28:53.000	16.278	1.432	2436.836993
	14 May 2019 11:29:22.305	13.253	-0.124	2605.248095
Min Elevation	14 May 2019 11:29:22.305	13.253	-0.124	2605.248163
Max Elevation	14 May 2019 11:24:37.997	68.829	12.511	1554.311051
Mean Elevation			6.218	
Min Range	14 May 2019 11:24:37.873	68.865	12.511	1554.310781
Max Range	14 May 2019 11:29:22.305	13.253	-0.124	2605.248163
Mean Range				2034.650505

	Time (UTCG)	Azimuth (deg)	Elevation (deg)	Range (km)
	14 May 2019 12:52:27.676	187.107	-0.124	2599.613628
	14 May 2019 12:53:27.000	190.630	3.784	2199.756295
	14 May 2019 12:54:27.000	195.783	8.546	1807.772327
	14 May 2019 12:55:27.000	203.861	14.566	1440.848390
	14 May 2019 12:56:27.000	217.730	22.228	1126.055208
	14 May 2019 12:57:27.000	242.406	29.926	920.447037
	14 May 2019 12:58:27.000	276.465	30.768	902.922720
	14 May 2019 12:59:27.000	303.275	23.641	1082.560796
	14 May 2019 13:00:27.000	318.579	15.764	1383.929454
	14 May 2019 13:01:27.000	327.406	9.499	1743.994324
	14 May 2019 13:02:27.000	332.994	4.574	2131.959421
	14 May 2019 13:03:27.000	336.848	0.524	2533.636807
	14 May 2019 13:03:37.578	337.409	-0.124	2605.279615

Min Elevation	14 May 2019 13:03:37.578	337.409	-0.124	2605.279618
Max Elevation	14 May 2019 12:58:02.007	262.123	31.701	883.913652
Mean Elevation			12.582	
Min Range	14 May 2019 12:58:01.926	262.076	31.701	883.913453
Max Range	14 May 2019 13:03:37.578	337.409	-0.124	2605.279618
Mean Range				1729.136617

Time (UTCG)	Azimuth (deg)	Elevation (deg)	Range (km)
15 May 2019 00:25:15.987	25.472	-0.124	2587.471760
15 May 2019 00:26:15.000	29.825	3.612	2201.299400
15 May 2019 00:27:15.000	36.082	8.084	1825.286515
15 May 2019 00:28:15.000	45.551	13.476	1481.269664
15 May 2019 00:29:15.000	60.704	19.669	1199.520478
15 May 2019 00:30:15.000	84.232	24.692	1034.250726
15 May 2019 00:31:15.000	112.511	24.332	1043.465450
15 May 2019 00:32:15.000	135.168	18.953	1223.398304
15 May 2019 00:33:15.000	149.575	12.762	1513.922433
15 May 2019 00:34:15.000	158.577	7.444	1863.182955
15 May 2019 00:35:15.000	164.528	3.032	2242.824680
15 May 2019 00:36:04.843	168.094	-0.124	2570.781689

Min Elevation	15 May 2019 00:36:04.843	168.094	-0.124	2570.781689
Max Elevation	15 May 2019 00:30:41.718	96.877	25.370	1014.975405
Mean Elevation			11.317	
Min Range	15 May 2019 00:30:42.049	97.036	25.369	1014.972501
Max Range	15 May 2019 00:25:15.987	25.472	-0.124	2587.471760
Mean Range				1732.222838

Time (UTCG)	Azimuth (deg)	Elevation (deg)	Range (km)
15 May 2019 01:59:16.592	349.448	-0.124	2588.319194
15 May 2019 02:00:16.000	343.398	3.258	2235.690130
15 May 2019 02:01:16.000	334.979	6.945	1913.114901
15 May 2019 02:02:16.000	323.246	10.687	1645.947161
15 May 2019 02:03:16.000	307.447	13.749	1466.202793
15 May 2019 02:04:16.000	288.541	14.844	1408.565122
15 May 2019 02:05:16.000	269.953	13.307	1487.429539
15 May 2019 02:06:16.000	254.800	10.028	1683.292826
15 May 2019 02:07:16.000	243.640	6.247	1960.575575
15 May 2019 02:08:16.000	235.605	2.591	2288.774572

	15 May 2019 02:08:16.000	235.605	2.591	2288.774572
	15 May 2019 02:09:03.925	230.774	-0.124	2573.697154
Min Elevation	15 May 2019 01:59:16.592	349.448	-0.124	2588.319194
Max Elevation	15 May 2019 02:04:10.678	290.266	14.855	1408.125793
Mean Elevation			7.401	
Min Range	15 May 2019 02:04:11.170	290.106	14.855	1408.120207
Max Range	15 May 2019 01:59:16.592	349.448	-0.124	2588.319194
Mean Range				1931.964452

Section Statistics

Min Elevation	14 May 2019 11:29:22.305	13.253	-0.124	2605.248163
Max Elevation	14 May 2019 12:58:02.007	262.123	31.701	883.913652
Mean Elevation			9.557	
Min Range	14 May 2019 12:58:01.926	262.076	31.701	883.913453
Max Range	14 May 2019 13:03:37.578	337.409	-0.124	2605.279618
Mean Range				1848.898183

	15 May 2019 02:01:30.849	225.164	-0.124	2567.543897
Min Elevation	15 May 2019 01:51:18.785	352.692	-0.124	2584.167035
Max Elevation	15 May 2019 01:56:25.427	289.098	18.490	1240.947792
Mean Elevation			8.426	
Min Range	15 May 2019 01:56:25.908	288.917	18.490	1240.942673
Max Range	15 May 2019 01:51:18.785	352.692	-0.124	2584.167035
Mean Range				1878.745708

Section Statistics

Min Elevation	14 May 2019 12:44:38.480	181.939	-0.124	2601.395754
Max Elevation	14 May 2019 12:50:18.915	261.054	40.807	739.575804
Mean Elevation			9.745	
Min Range	14 May 2019 12:50:18.875	261.023	40.807	739.575750
Max Range	14 May 2019 11:21:28.150	16.835	-0.124	2605.379991
Mean Range				1853.315635

APPENDIX B

REPORT ACCESS OF SCENARIO 2 IN STK

Facility-KyutechGS-To-Satellite-LEMUR-2-XUENITERENCE_42772

KyutechGS-To-LEMUR-2-XUENITERENCE_42772 - AER reported in the object's default AER frame

	Time (UTCG)	Azimuth (deg)	Elevation (deg)	Range (km)
	14 May 2019 10:40:38.124	94.502	-0.124	2581.103062
	14 May 2019 10:41:38.000	84.888	1.590	2399.614351
	14 May 2019 10:42:38.000	73.971	2.735	2287.324101
	14 May 2019 10:43:38.000	62.326	3.092	2255.774726
	14 May 2019 10:44:38.000	50.792	2.584	2308.552867
	14 May 2019 10:45:38.000	40.169	1.325	2440.081927
	14 May 2019 10:46:27.643	32.411	-0.124	2599.847054
Min Elevation	14 May 2019 10:46:27.643	32.411	-0.124	2599.847054
Max Elevation	14 May 2019 10:43:32.645	63.374	3.095	2255.150118
Mean Elevation			1.582	
Min Range	14 May 2019 10:43:30.368	63.819	3.095	2255.090150
Max Range	14 May 2019 10:46:27.643	32.411	-0.124	2599.847054
Mean Range				2410.328298

	Time (UTCG)	Azimuth (deg)	Elevation (deg)	Range (km)
	14 May 2019 12:10:48.407	165.630	-0.124	2565.198001
	14 May 2019 12:11:48.000	165.394	4.089	2139.915450
	14 May 2019 12:12:48.000	164.994	9.479	1714.660271
	14 May 2019 12:13:48.000	164.244	17.119	1298.076526
	14 May 2019 12:14:48.000	162.507	29.898	905.342065
	14 May 2019 12:15:48.000	155.613	56.125	589.713535
	14 May 2019 12:16:48.000	13.697	72.567	520.884385
	14 May 2019 12:17:48.000	354.338	38.020	768.423909
	14 May 2019 12:18:48.000	351.682	21.517	1141.734618
	14 May 2019 12:19:48.000	350.724	12.417	1551.478729
	14 May 2019 12:20:48.000	350.291	6.348	1973.777592
	14 May 2019 12:21:48.000	350.090	1.748	2400.557022
	14 May 2019 12:22:16.438	350.043	-0.124	2603.296986
Min Elevation	14 May 2019 12:22:16.438	350.043	-0.124	2603.297021
Max Elevation	14 May 2019 12:16:29.779	77.671	82.187	502.672855
Mean Elevation			20.698	
Min Range	14 May 2019 12:16:29.586	78.918	82.186	502.670812

Max Range	14 May 2019 12:22:16.438	350.043	-0.124	2603.297021
Mean Range				1551.773776

	Time (UTCG)	Azimuth (deg)	Elevation (deg)	Range (km)
	14 May 2019 13:47:38.604	238.413	-0.124	2573.111318
	14 May 2019 13:48:38.000	247.976	1.583	2392.410470
	14 May 2019 13:49:38.000	258.911	2.773	2275.910360
	14 May 2019 13:50:38.000	270.625	3.215	2236.423515
	14 May 2019 13:51:38.000	282.328	2.822	2277.885000
	14 May 2019 13:52:38.000	293.241	1.683	2395.684012
	14 May 2019 13:53:38.000	302.877	0.008	2578.684831
	14 May 2019 13:53:42.224	303.502	-0.124	2593.672222
Min Elevation	14 May 2019 13:47:38.604	238.413	-0.124	2573.111318
Max Elevation	14 May 2019 13:50:39.714	270.963	3.216	2236.486781
Mean Elevation			1.479	
Min Range	14 May 2019 13:50:37.230	270.472	3.215	2236.416789
Max Range	14 May 2019 13:53:42.224	303.502	-0.124	2593.672223
Mean Range				2415.472716

	Time (UTCG)	Azimuth (deg)	Elevation (deg)	Range (km)
	14 May 2019 23:44:25.557	40.453	-0.124	2630.571565
	14 May 2019 23:45:25.000	47.915	2.709	2331.589016
	14 May 2019 23:46:25.000	57.482	5.510	2072.962325
	14 May 2019 23:47:25.000	69.454	7.935	1877.212084
	14 May 2019 23:48:25.000	83.642	9.453	1766.586724
	14 May 2019 23:49:25.000	98.872	9.556	1757.984152
	14 May 2019 23:50:25.000	113.331	8.196	1853.086967
	14 May 2019 23:51:25.000	125.681	5.838	2037.251790
	14 May 2019 23:52:25.000	135.586	3.033	2288.563330
	14 May 2019 23:53:25.000	143.350	0.137	2586.748441
	14 May 2019 23:53:30.461	143.967	-0.124	2615.643118
Min Elevation	14 May 2019 23:53:30.461	143.967	-0.124	2615.643121
Max Elevation	14 May 2019 23:48:59.019	92.263	9.703	1748.649905
Mean Elevation			4.738	
Min Range	14 May 2019 23:48:59.852	92.476	9.702	1748.639028
Max Range	14 May 2019 23:44:25.557	40.453	-0.124	2630.571565
Mean Range				2165.290865

	Time (UTCG)	Azimuth (deg)	Elevation (deg)	Range (km)
	15 May 2019 01:17:09.683	2.327	-0.124	2631.201743
	15 May 2019 01:18:09.000	359.868	3.872	2221.282696
	15 May 2019 01:19:09.000	356.120	8.817	1815.075000
	15 May 2019 01:20:09.000	349.959	15.293	1427.153128
	15 May 2019 01:21:09.000	338.528	24.285	1080.057111
	15 May 2019 01:22:09.000	314.501	35.473	829.233418
	15 May 2019 01:23:09.000	272.755	38.904	775.992366
	15 May 2019 01:24:09.000	240.193	28.995	954.164667
	15 May 2019 01:25:09.000	224.579	18.698	1269.222369
	15 May 2019 01:26:09.000	216.624	11.254	1643.274323
	15 May 2019 01:27:09.000	211.970	5.740	2042.945056
	15 May 2019 01:28:09.000	208.944	1.363	2454.365795
	15 May 2019 01:28:32.131	208.044	-0.124	2614.605107
Min Elevation	15 May 2019 01:28:32.131	208.044	-0.124	2614.605429
Max Elevation	15 May 2019 01:22:51.834	285.364	39.662	765.758300
Mean Elevation			14.803	
Min Range	15 May 2019 01:22:52.017	285.227	39.662	765.757093
Max Range	15 May 2019 01:17:09.683	2.327	-0.124	2631.201743
Mean Range				1673.736368

Section Statistics

Min Elevation	14 May 2019 12:22:16.438	350.043	-0.124	2603.297021
Max Elevation	14 May 2019 12:16:29.779	77.671	82.187	502.672855
Mean Elevation			10.318	
Min Range	14 May 2019 12:16:29.586	78.918	82.186	502.670812
Max Range	15 May 2019 01:17:09.683	2.327	-0.124	2631.201743
Mean Range				1960.498292

APPENDIX C

REPORT ACCESS OF SCENARIO 3 IN STK

Facility-KyutechGS-To-Satellite--LEMUR-2-NOGUECORREIG_41996

KyutechGS-To-LEMUR-2-NOGUECORREIG_41996 - AER reported in the object's default AER frame

	Time (UTCG)	Azimuth (deg)	Elevation (deg)	Range (km)
	14 May 2019 03:08:57.547	326.688	-0.124	2601.709451
	14 May 2019 03:09:57.000	317.215	1.503	2423.906872
	14 May 2019 03:10:57.000	306.413	2.568	2313.630355
	14 May 2019 03:11:57.000	294.914	2.854	2283.270533
	14 May 2019 03:12:57.000	283.529	2.297	2335.948276
	14 May 2019 03:13:57.000	273.021	1.014	2465.988096
	14 May 2019 03:14:36.609	266.797	-0.124	2588.533991
Min Elevation	14 May 2019 03:08:57.547	326.688	-0.124	2601.709451
Max Elevation	14 May 2019 03:11:47.198	296.807	2.865	2282.528432
Mean Elevation			1.427	
Min Range	14 May 2019 03:11:48.828	296.492	2.865	2282.496602
Max Range	14 May 2019 03:08:57.547	326.688	-0.124	2601.709451
Mean Range				2430.426796

	Time (UTCG)	Azimuth (deg)	Elevation (deg)	Range (km)
	14 May 2019 12:06:31.514	138.742	-0.124	2568.880247
	14 May 2019 12:07:31.000	133.923	3.622	2186.841520
	14 May 2019 12:08:31.000	126.961	7.994	1823.718917
	14 May 2019 12:09:31.000	116.488	13.044	1501.471219
	14 May 2019 12:10:31.000	100.419	18.288	1254.124316
	14 May 2019 12:11:31.000	77.764	21.607	1133.374241
	14 May 2019 12:12:31.000	53.246	20.350	1179.438947
	14 May 2019 12:13:31.000	34.003	15.690	1375.555064
	14 May 2019 12:14:31.000	21.235	10.461	1669.025079
	14 May 2019 12:15:31.000	12.913	5.794	2016.835070
	14 May 2019 12:16:31.000	7.280	1.773	2394.236248
	14 May 2019 12:17:02.466	5.028	-0.124	2599.226223
Min Elevation	14 May 2019 12:17:02.466	5.028	-0.124	2599.226528
Max Elevation	14 May 2019 12:11:45.553	71.666	21.760	1128.755887
Mean Elevation			9.865	
Min Range	14 May 2019 12:11:44.818	71.975	21.760	1128.742773
Max Range	14 May 2019 12:17:02.466	5.028	-0.124	2599.226528

Mean Range				1808.560591

	Time (UTCG)	Azimuth (deg)	Elevation (deg)	Range (km)
	14 May 2019 13:40:09.067	201.463	-0.124	2565.707633
	14 May 2019 13:41:09.000	207.358	3.419	2203.047707
	14 May 2019 13:42:09.000	215.509	7.355	1869.237550
	14 May 2019 13:43:09.000	227.054	11.557	1585.044344
	14 May 2019 13:44:09.000	243.164	15.344	1382.792388
	14 May 2019 13:45:09.000	263.396	17.160	1302.039151
	14 May 2019 13:46:09.000	283.957	15.832	1364.627505
	14 May 2019 13:47:09.000	300.723	12.286	1552.853324
	14 May 2019 13:48:09.000	312.853	8.143	1827.442670
	14 May 2019 13:49:09.000	321.440	4.201	2154.504143
	14 May 2019 13:50:09.000	327.666	0.639	2512.330065
	14 May 2019 13:50:22.705	328.849	-0.124	2596.917893
Min Elevation	14 May 2019 13:50:22.705	328.849	-0.124	2596.918155
Max Elevation	14 May 2019 13:45:13.897	265.131	17.172	1301.751102
Mean Elevation			7.974	
Min Range	14 May 2019 13:45:12.886	264.772	17.171	1301.730136
Max Range	14 May 2019 13:50:22.705	328.849	-0.124	2596.918155
Mean Range				1909.712031

	Time (UTCG)	Azimuth (deg)	Elevation (deg)	Range (km)
	15 May 2019 01:10:53.891	17.791	-0.124	2602.818535
	15 May 2019 01:11:53.000	20.022	3.881	2190.888501
	15 May 2019 01:12:53.000	23.278	8.918	1778.555627
	15 May 2019 01:13:53.000	28.518	15.697	1380.122431
	15 May 2019 01:14:53.000	38.460	25.743	1015.138656
	15 May 2019 01:15:53.000	62.277	40.348	738.184972
	15 May 2019 01:16:53.000	114.583	46.167	671.240450
	15 May 2019 01:17:53.000	152.049	32.103	865.027780
	15 May 2019 01:18:53.000	166.641	19.721	1198.783158
	15 May 2019 01:19:53.000	173.523	11.600	1585.631976
	15 May 2019 01:20:53.000	177.472	5.845	1993.784113
	15 May 2019 01:21:53.000	180.043	1.369	2411.144504
	15 May 2019 01:22:15.905	180.806	-0.124	2571.648741
Min Elevation	15 May 2019 01:10:53.891	17.791	-0.124	2602.818535

Max Elevation	15 May 2019 01:16:37.173	99.405	47.236	661.351012
Mean Elevation			16.242	
Min Range	15 May 2019 01:16:37.438	99.665	47.236	661.348010
Max Range	15 May 2019 01:10:53.891	17.791	-0.124	2602.818535
Mean Range				1615.613034

	Time (UTCG)	Azimuth (deg)	Elevation (deg)	Range (km)
	15 May 2019 02:45:26.929	340.918	-0.124	2602.696056
	15 May 2019 02:46:26.000	333.245	2.616	2312.016402
	15 May 2019 02:47:26.000	323.314	5.240	2066.990775
	15 May 2019 02:48:26.000	311.021	7.335	1893.416764
	15 May 2019 02:49:26.000	296.849	8.381	1812.697081
	15 May 2019 02:50:26.000	282.204	8.013	1837.362854
	15 May 2019 02:51:26.000	268.779	6.363	1963.219976
	15 May 2019 02:52:26.000	257.561	3.926	2172.133578
	15 May 2019 02:53:26.000	248.643	1.173	2441.966637
	15 May 2019 02:53:53.705	245.205	-0.124	2581.676204
Min Elevation	15 May 2019 02:45:26.929	340.918	-0.124	2602.696056
Max Elevation	15 May 2019 02:49:40.807	293.209	8.426	1808.845297
Mean Elevation			4.280	
Min Range	15 May 2019 02:49:42.115	292.887	8.426	1808.819720
Max Range	15 May 2019 02:45:26.929	340.918	-0.124	2602.696056
Mean Range				2168.417633

Section Statistics

Min Elevation	14 May 2019 13:50:22.705	328.849	-0.124	2596.918155
Max Elevation	15 May 2019 01:16:37.173	99.405	47.236	661.351012
Mean Elevation			8.852	
Min Range	15 May 2019 01:16:37.438	99.665	47.236	661.348010
Max Range	15 May 2019 01:10:53.891	17.791	-0.124	2602.818535
Mean Range				1931.840830